GeoScienceWorld
Lithosphere
Volume 2021, Article ID 7866186, 20 pages
https://doi.org/10.2113/2021/7866186

Lithosphere

Research Article

Synsedimentary to Diagenetic Cu ± Co Mineralization in Mesoproterozoic Pyritic Shale Driven by Magmatic-Hydrothermal Activity on the Edge of the Great Falls Tectonic Zone–Black Butte, Helena Embayment, Belt-Purcell Basin, USA: Evidence from Sulfide Re-Os Isotope Geochemistry

Nicolas J. Saintilan,[1,2] **Thomas E. Sheldrake**,[3] **Robert A. Creaser**,[1] **David Selby**,[2,4] **Jerry Zieg**,[5] **Adrian Boyce**,[6] **and Cyril Chelle-Michou**[7]

[1]*Department of Earth and Atmospheric Sciences, University of Alberta, Edmonton, Alberta, Canada T6G 2E3*
[2]*Department of Earth Sciences, University of Durham, Durham DH1 3LE, UK*
[3]*Department of Earth Sciences, University of Geneva, Rue des Maraîchers 13, 1205 Geneva, Switzerland*
[4]*State Key Laboratory of Geological Processes and Mineral Resources, School of Earth Resources, China University of Geosciences, Wuhan, China 430074*
[5]*Sandfire Resources America Inc., Tintina Montana Inc., 17 East Main Street, P.O. Box 431, White Sulphur Springs, MT, USA 59645*
[6]*Scottish Universities Environmental Research Centre, Rankine Avenue, East Kilbride, G75 0QF Glasgow, UK*
[7]*Institute of Geochemistry and Petrology, Department of Earth Sciences, ETH Zürich, Clausiusstrasse 25, 8092 Zürich, Switzerland*

Correspondence should be addressed to Nicolas J. Saintilan; nicolas.saintilan@erdw.ethz.ch

Received 13 January 2021; Accepted 15 April 2021; Published 17 June 2021

Academic Editor: Patricia Durance

The ca. 1,500 to 1,325 Ma Mesoproterozoic Belt-Purcell Basin is an exceptionally preserved archive of Mesoproterozoic Earth and its paleoenvironmental conditions. The Belt-Purcell Basin is also host to world-class base metal sediment-hosted mineralization produced in a variety of settings from the rift stage of basin evolution through the subsequent influence of East Kootenay and Grenvillian orogenies. The mineral potential of this basin has not been fully realized yet. New rhenium-osmium (Re-Os) data presented here for chalcopyrite, pyrite, and black shale contribute to refine a robust genetic model for the origin of the Black Butte copper ± cobalt ± silver (Cu ± Co ± Ag) deposit hosted by the ca. >1,475 Ma Newland Formation in the Helena Embayment of the Belt-Purcell Basin in Montana, USA. Chalcopyrite Re-Os data yield an isochron age (1,488 ± 34 Ma, unradiogenic initial $^{187}Os/^{188}Os$ composition $Os_{i\text{-}chalcopyrite} = 0.13 \pm 0.11$) that overlaps with the geological age of the Newland Formation. Further, the Re-Os data of synsedimentary to diagenetic massive pyrite yield evidence of resetting with an isochron age (1,358 ± 42 Ma) coincident with the timing of the East Kootenay orogeny. The unradiogenic $Os_{i\text{-}chalcopyrite}$ at ca. 1,488 Ma (0.13 ± 0.11) argues for derivation of Os from a magmatic source with a $^{187}Os/^{188}Os$ isotopic composition inherited from the upper mantle in the Mesoproterozoic ($Os_{mantle\,1{,}475\,Ma} = 0.12 \pm 0.02$). The unradiogenic $Os_{i\text{-}chalcopyrite}$ also suggests limited contamination from a continental crustal source. This source of Os and our new sulfur isotopic signatures of chalcopyrite (−4.1 to +2.1‰-VCDT) implies a dominantly magmatic source for metals. We integrate our new results and previously published geological and geochemical evidence to conceptualize a genetic model in which Cu and metals were largely contributed by moderate-temperature, reduced magmatic-hydrothermal fluids carrying reduced sulfur species with a magmatic origin and flowing as highly metalliferous fluids within the shale sequence. A subsidiary derivation of metals during thermally forced shale diagenesis is possible. Chalcopyrite mineralization replaced locally massive synsedimentary to diagenetic pyrite units close to the sediment-water interface, i.e., an ideal locus where magmatic-hydrothermal fluids could cool and the solubility of chalcopyrite would fall. We suggest that Cu mineralization was coeval with the timing of an enhanced thermal gradient in the Helena Embayment triggered until ca. 1,455 Ma by tholeiitic dike swarm that intruded into Archean basement rocks and intersected the NE-SW-trending Great Falls Tectonic Zone.

1. Introduction

A comprehensive knowledge of the timing and lithostratigraphic position of hydrothermal fluid flow and mineralization processes throughout the sedimentary infill of intracontinental rifts is paramount in the identification of sedimentary basins that may contain giant sediment-hosted base metal mineralization (e.g., [1]). The preponderance of strata-bound massive pyrite deposits with economic concentrations of base metals (copper (Cu), zinc (Zn), and lead (Pb)) within Mesoproterozoic strata has been tied to increasing marine concentrations of sulfate following the rise of atmospheric oxygen [2–6]. In a graben extending eastward from the center of the Mesoproterozoic Belt-Purcell Basin, Canada-USA (Helena Embayment; Figure 1), the Black Butte (formerly known as Sheep Creek) copper ± cobalt ± silver (Cu ± Co ± Ag) deposit is hosted by massive pyritic shale of the Newland Formation. The Black Butte deposit is thought to have formed during diagenesis in connection with the interaction between biogenically and/or thermally sourced reduced sulfur and metalliferous hydrothermal fluids during basin development [6, 7].

The conceptualization of a genetic model for base metal sediment-hosted deposits is based on the identification of six key components: (i) the origin of fluids and their chemistry (redox conditions—reduced versus oxidized fluids, temperatures, and type of ligand to transport metals); (ii) the source(s) of metals (e.g., Cu, Zn, and Pb ± Co ± Ag); (iii) the trigger(s) for a decrease of the solubility of metals; (iv) a reducing agent and/or source of reduced sulfur to fix the metals, in particular in the case of oxidized metalliferous fluids; (v) a geodynamic engine responsible for fluid flow and convergence of the components listed above for the mineralizing processes, and (vi) the absolute timing of base metal mineralization that holds a central role in connecting points (i) to (v). Here, we attempt to constrain the timing of chalcopyrite mineralization and the source of metals as well as assess possible controls on mineralization exerted by (i) continental tholeiitic magmatism coeval with the development of the Belt-Purcell intracontinental rift and (ii) tectonic structures in the long-lived Great Falls Tectonic Zone (GFTZ) in the Archean Wyoming Province, on the southern edge of the Helena Embayment. To this end, we present new petrographic evidence, Re-Os and sulfur isotope data for chalcopyrite associated with massive pyrite beds and intercalated black shale and siltstone, complemented by new Re-Os isotope data for the host pyritic shale sequence at Black Butte.

2. Regional Geological Setting and Paleoenvironmental Conditions of Sedimentation and Sulfide Precipitation

2.1. Basin Development on the Rifted Margins of the Nuna Supercontinent. In west-central Montana, massive pyrite units interbedded with black shale, which experienced subgreenschist-facies metamorphic conditions during the ca. 1,370 to 1,325 Ma East Kootenay orogeny [8–11], extend over 25 km along the Volcano Valley-Buttress fault system, and 8 km southward in the Newland Formation within a structural block along a major bend in the fault system (Figure 2(a)) [7]. This structural block is located on the northern margin of the Helena Embayment, which is an asymmetric, E-NE-trending branch of the main Mesoproterozoic Belt-Purcell Basin in Canada and the USA (Figure 1) [12]. The Belt-Purcell Basin was initiated at ca. 1,500 to 1,485 Ma as an intracontinental rift during breakup of the Nuna supercontinent [1, 13, 14]. The Helena Embayment comprises a shallow carbonate shelf in the north, with a southern edge related to a steep and active fault scarp against the uplifted basement of the Archean Wyoming Province [12]. A NW-trending, low-K tholeiitic dike swarm dated at ca. 1,455 Ma (i.e., currently available best age estimate from whole-rock Rb-Sr geochronology) lies within Archean basement rocks to the south of the Helena Embayment and the Belt-Purcell Basin (Figure 1) [12, 15]. The dike swarm has the same strike orientation as ca. 1,468 Ma gabbroic sills found in rift-facies marine turbidites in the main Belt-Purcell Basin, in particular within footwall sediments of the ca. 1,475 Ma synsedimentary Sullivan deposit (U-Pb TIMS cassiterite geochronology, [16]) hosted in the Lower Aldridge Formation, southeastern British Columbia, Canada (Figure 1) [1, 17, 18]. The Newland Formation is interpreted as (1) being slightly younger than the Prichard Formation (i.e., lateral equivalent to the Lower Aldridge Formation) and (2) older than the >1,454 Ma Revett Formation (SHRIMP U-Pb geochronology of bentonite) [19] in northwestern Montana and Idaho in the main Belt-Purcell Basin ([20]; detailed stratigraphic correlations in [7], their Figure 2). In light of these stratigraphic correlations with the northernmost and westernmost part of the main Belt-Purcell basin, maximum and minimum ages of ca. 1,470 and 1,454 Ma have been reported and utilized for the Newland Formation in previous works [7]. However, new detrital zircon U-Pb geochronology data from the northern tip of the main Belt-Purcell basin in British Columbia suggest that the deposition of the Creston Formation, which overlies the Upper Aldridge Formation [7], was rapid between ca. 1,475 and 1,467 Ma [21]. The base of the Creston Formation is directly correlated with the base of the Spokane Formation which overlies the Newland Formation in the northern Helena Embayment, in particular in the Black Butte area. Therefore, the Newland Formation may be older than ca. 1,475 Ma.

2.2. Paleoenvironmental Conditions and Sedimentation in an Anoxic but Sulfate-Bearing Mesoproterozoic Marine Environment. Sedimentary rocks of the Newland Formation were deposited in a subtidal setting during active subsidence and synsedimentary tectonism along W-trending, basin-bounding faults in the Helena Embayment (Figures 1 and 2(a)) [7, 12]. In addition, N-trending synsedimentary faults steered debris-flow sedimentation that, in turn, controlled fluid flow and the formation of synsedimentary to early diagenetic massive to bedded fine-grained pyrite units within topographic lows flanked by shale horsts (Figure 2(a)) [7]. The sedimentary to early diagenetic nature of the fine-grained pyrite units is supported by the petrography of both matrix- and clast-supported sedimentary breccias that

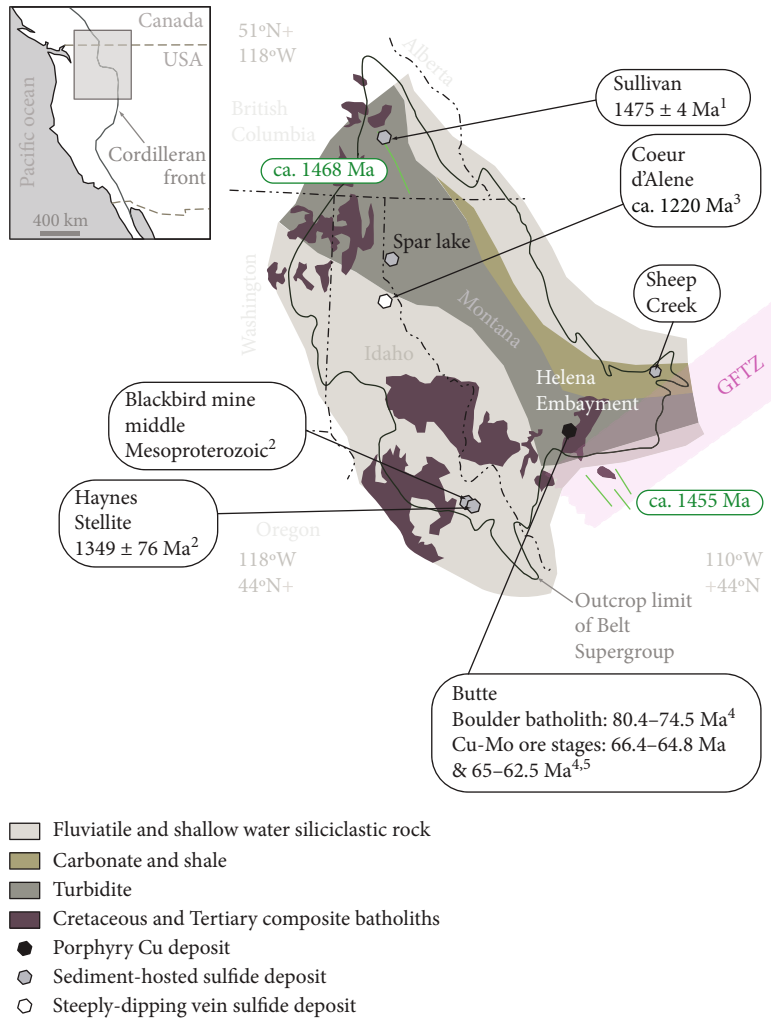

Figure 1: Simplified geological map of sedimentary facies distribution of the lower Belt Supergroup in the Belt-Purcell Basin in Canada and the USA. Positions of ca. 1,468 Ma gabbroic sills in footwall of the Sullivan deposit and ca. 1,455 Ma tholeiitic dikes in Archean basement are shown (modified from [1]). Map shows location of major mineral deposits including mineralization ages where available (after [1][16]; [2][39]; [3][89]; [4][90]; [5][91]). Abbreviation: GFTZ: Great Falls Tectonic Zone (location after [70]).

contain poorly sorted, angular, granule- to cobble-sized clasts of the laminated striped shale and pyrite strata, including clasts of broken, pyrite-walled tube structures (Figure 2(b), e.g., sample 28-SC) [6, 7]. The microlaminated, organic-rich black shale of the Newland Formation (1.1 to 1.4 wt.% C at the Black Butte deposit, 0.1 to 3.4 wt.% C outside the Cu-mineralized areas) [9] is interbedded with centimeter-scale homogeneous muddy turbidites [9]. Collectively, these facies record deep-water, organic-rich sedimentation [22, 23].

Outside of the massive sulfide zones, black shale contains ubiquitous, disseminated pyrite framboids and finely crystalline pyrite blebs within laminae characterized by compactional draping of pyrite framboids [9]. The broad range of $\delta^{34}S$ values of disseminated pyrite (–8.7‰ to +36.3‰ versus the Vienna Cañon Diablo Troilite (VCDT)) may be compatible with bacterial mechanisms of sulfate reduction [9]. The redox conditions for the mid-Proterozoic ocean suggest that the deposition of the Newland Formation took place in an anoxic but sulfate-bearing (2–6 mM) water column [6, 24–26]. The discharge from vents of metalliferous hydrothermal fluids into the overlying, predominantly sulfidic water column resulted in the formation of decimeter-scale tubular structures with pyrite walls [6]. Those vents, which released saline hydrothermal fluids denser than seawater (cf. [27] in [6]), were populated by sulfate-reducing bacteria [9, 28, 29]. At the sediment-water interface on the seafloor of the Helena Embayment, the interplay between those sulfate-reducing organisms and vents of metalliferous hydrothermal fluids steered the dynamics and redox conditions of bottom waters (i.e., transition from episodic sulfate-rich waters due to episodic marine input to predominantly sulfate-poor sulfidic waters) [6].

2.3. Sequence of Mineral Precipitation, Sulfur Isotope Composition, and Basin Hydrodynamics. Deposition of abundant disseminated pyrite ($\delta^{34}S$ = –8.7 to +36.3‰) [9] and pyrite nodules (modal $\delta^{34}S$ at ca. –5.0‰, with values as low as –18.0‰ illustrating kinetic fractionation triggered by microbial sulfate reduction in an open system) [6, 30],

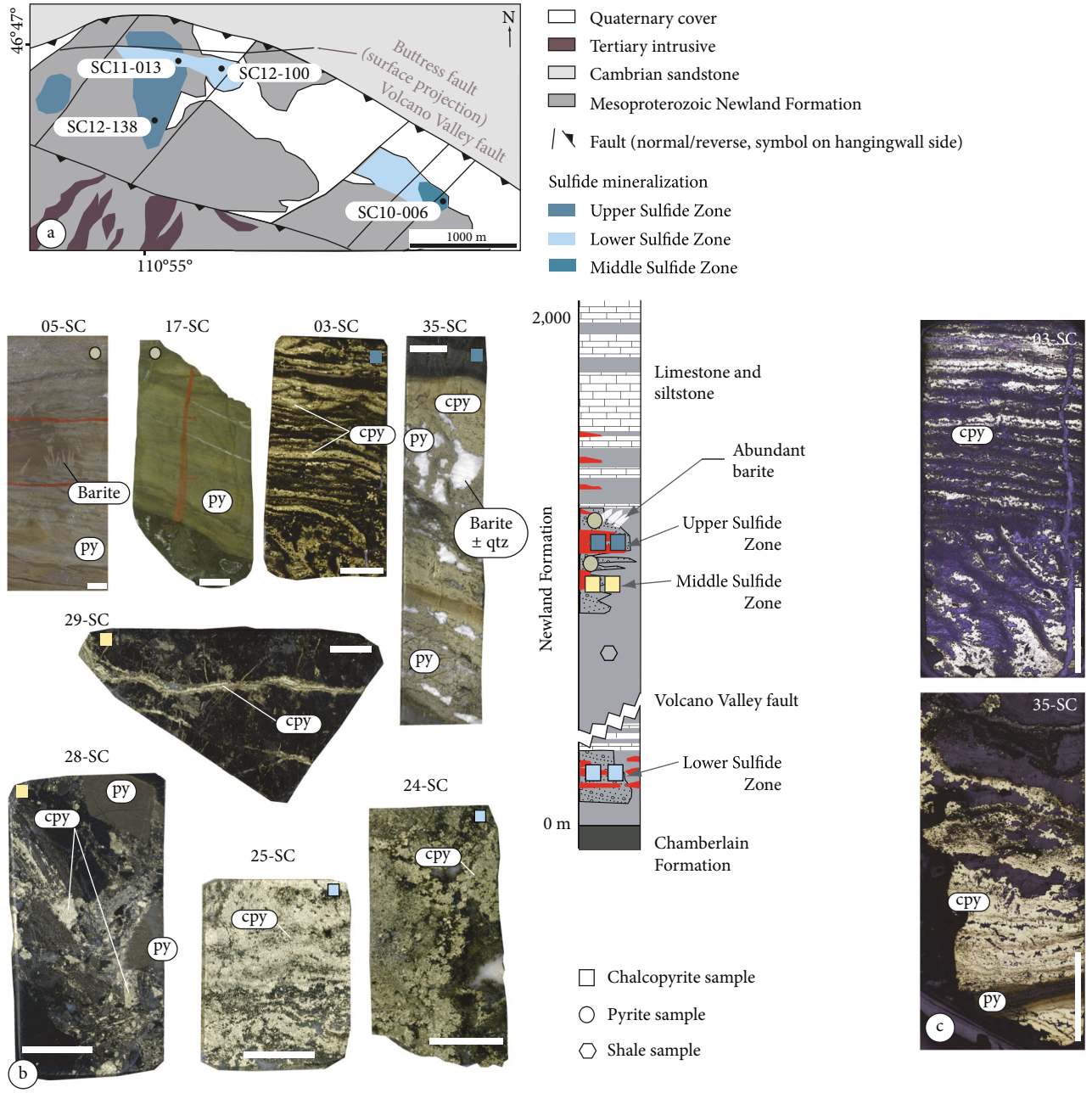

FIGURE 2: (a) Geological map of the Black Butte deposit (modified from [7] and references therein) showing locations of drill cores from which samples analyzed in this study were taken (Table 1). (b) Stratigraphic column at Black Butte including the Newland Formation in the lower Belt Supergroup (after [7]). Stratigraphic levels of the samples processed and analyzed in this study are shown on the column. The scans of the drill cores for each chalcopyrite-bearing and/or pyrite-bearing sample are displayed. Sample 05-SC corresponds to massive pyrite units atop the Upper Sulfide Zone. Abbreviations: py: pyrite; cpy: chalcopyrite. All scale bars are 1 cm long. (c) High-resolution scan (reflected light microphotographs) of representative chalcopyrite mineralization showing no signs of recrystallization. All scale bars are 1 cm long.

which formed within the surface sediments, characterize the sedimentary and syndiagenetic stage at Black Butte [6]. Early diagenetic barite laths in the laminated black shale ($\delta^{34}S = +14.0$ to $+18.0‰$) [6] precipitated below the sediment-water interface from residual pore-fluid sulfate enriched in ^{34}S as a result of excess of sulfate reduction with respect to the diffusion of sulfate from coeval seawater ($\delta^{34}S = +10.0$ to $+12.0‰$) into sediments [6, 30].

A second stage of mineral precipitation coincided with formation of the tube walls with rapid replacement by mottled ($\delta^{34}S_{mean} = +10.3 \pm 12.5‰$, 1 standard deviation (SD), $n = 108$, up to $+45‰$) and colloform ($\delta^{34}S = +10.8 \pm 7.1‰$, 1 SD, $n = 63$, up to $+34.0‰$) pyrite [6]. Rare euhedral marcasite, hypothetically indicating some biogenically induced, transient, locally acidic and oxic conditions [6, 31–33], overgrows the pyrite walls. The sulfur isotopic composition of

colloform and mottled pyrite is consistent with quantitative reduction of seawater sulfate that, in turn, favors pyrite precipitation steered by the iron supply from hydrothermal fluids. With subsequent recharge of the water column in sulfate via oxic seawater ingress from the main Belt-Purcell Basin, a rejuvenation of the activity of sulfate-reducing bacteria took place, thereby inducing mottled pyrite precipitation with highly variable sulfur isotopic compositions [6].

In a third stage, massive barite filled the tube structures and was in turn replaced by dolomite and quartz (Figure 2(b)). In the fourth and final stage, with increased burial and depth of mineralization within the sedimentary sequence, barite, quartz, dolomite, and all earlier pyrite generations were replaced by base metal sulfides (chalcopyrite: $\delta^{34}S_{mean}$ = −5.1 to +7.1‰; [34]; $\delta^{34}S_{mean}$ = +3.9 ± 1.2‰, 1 SD, n = 5; [6]) and coarse-grained pyrite ($\delta^{34}S_{mean}$ = +6.1 ± 4.2‰, 1 SD, n = 97) [6] accompanied by silica [6, 7, 33]. The base metal paragenesis, which is suggested to have formed from hotter or more oxidizing mineralizing fluids [7], is marked by a stage of Co-sulfarsenides and Cu-sulfosalts that preceded chalcopyrite mineralization [7, 33]. Base metal sulfides have sulfur isotopic compositions (ca. −5.1 to +7.1‰) lighter than early mottled and colloform pyrite (ca. +10.3 ± 12.5‰, up to +45‰) and seawater sulfate at the time of deposition of the Newland Formation (+10.0 to +12.0‰) [6]. In contrast, massive barite, which is partly replaced by base metal sulfarsenides and sulfides, has the same sulfur isotopic composition as early diagenetic barite blades ($\delta^{34}S$ = +14.0 to +18.0‰; [6, 29, 35–37]). The sulfur isotopic composition of barite, coarse-grained pyrite, and base metal sulfides at Black Butte (stages 3 and 4) is interpreted as consistent with a process of thermal reduction of sulfate in barite. This process would yield H_2S with a sulfur isotopic composition ca. 10 to 20‰ lighter than sulfate in barite [6, 9]. However, a narrower range of $\delta^{34}S$ signatures clustering around 0‰ in chalcopyrite may be indicative of a contribution from a magmatic source of reduced sulfur for Cu mineralization [9, 34, 38]. Nonetheless, this magmatic contribution remains to be proven definitively and is discussed below.

2.4. Proposed Timing of Cu Mineralization. In the Belt-Purcell Basin, metalliferous hydrothermal and magmatic-hydrothermal fluids circulated in the main branch of this basin at least from the time of Zn-Pb-Ag mineralization in the Sullivan deposit at ca. 1,475 Ma (U-Pb TIMS cassiterite age) [16] to the time of magmatic-hydrothermal Cu-Co-Au mineralization at ca. 1,349 Ma in the Idaho cobalt belt (Re-Os isochron age of cobaltite) [39]. At Black Butte, Cu mineralization is restricted to the massive sulfide zones (Upper, Middle, and Lower Sulfide Zones; Figures 2(a) and 2(b)), in which massive pyrite layers are present [7, 9]. The black shale interbedded with massive pyrite beds is bereft of sulfides other than disseminated pyrite framboids and blebs of bacterial origin [9]. Not only does the black shale lack base metal sulfides (outside some rare replacement of disseminated pyrite by chalcopyrite) [40] but there is also no petrographic evidence for brittle-style veins and stockworks that could have formed as the result of fluids introduced epigenetically in the Newland Formation (Tintina Montana, Inc. staff, pers. comm., 2015).

Copper mineralization is proposed to have formed in the subsurface within the sedimentary sequence during continuous basin development and burial of the hydrothermal vents while diagenetic barite was being thermally reduced [6, 7]. Copper mineralization predates deformation and reactivation of the Volcano Valley fault during the Cretaceous to Paleocene Laramide orogeny [7, 19]. Therefore, the absolute age of the Cu ± Co ± Ag mineralization might span the timing of diagenesis of the Newland Formation and the transition to orogenic sedimentation and burial metamorphism during the East Kootenay orogeny and termination of sedimentation in the Belt-Purcell Basin [20, 41].

3. Material and Methods

3.1. Objectives and Selection of Samples. A total of six chalcopyrite-bearing samples, two pyrite samples, and one shale sample were collected from drill cores at the borehole archive of the Black Butte Copper deposit (Tintina Montana, Inc.) in Montana, USA (Table 1; Figures 2(a) and 2(b)). This study has determined the Re-Os isotope geochemistry of the six chalcopyrite samples from three pyrite zones that contain economically important Cu mineralization in the ca. 2000 m thick Newland Formation (Figures 2(a) and 2(b); Table 1): (1) the Lower Sulfide Zone (LSZ) in the footwall of the Volcano-Buttress fault system, which is at the base of the Newland Formation just above its contact with the Chamberlain Formation (samples NS-24-SC and NS-25-SC); (2) the Upper Sulfide Zone (USZ) in the hanging wall of the Volcano-Buttress fault system, above a package of carbonaceous shale overlying the Lower Sulfide Zone (samples NS-03-SC and NS-35-SC); and (3) the Middle Sulfide Zone (MSZ) located within shale immediately below the Upper Sulfide Zone (samples NS-28-SC and NS-29-SC). In addition, the Re-Os isotopic composition was determined on one pyrite sample from the massive fine-grained pyrite, between the MSZ and USZ, which formed during the earliest (i.e., synsedimentary) sulfide generation, and one fine-grained pyrite sample associated with barite at the top of the USZ. The shale sample, which lacks pyrite and chalcopyrite, was collected below the MSZ (Figure 2(b)); this sample was subdivided into two 5 cm long shale subsamples ("A, B," ca. 20 g each). The two shale subsamples were processed to determine their Re-Os isotopic composition in order to calculate the initial $^{187}Os/^{188}Os$ isotopic composition of the shale for the age interval proposed for deposition of the Newland Formation.

3.2. Sulfide Petrography and Quality Control of Mineral Separates. Polished thin sections of chalcopyrite- and/or pyrite-bearing samples were studied by transmitted and reflected light microscopy in order to establish paragenetic relationships. These relationships served as a basis for optimizing sample preparation, including determination of the step-wise methodology using a Frantz Isodynamic Separator at various currents to produce monomineralic mineral separates (see Section 3.3). After sample preparation, an aliquot

Table 1: Sample list with coordinates (latitude/longitude), geological characterization, and sections of drill cores from which samples were collected.

Lab number	Borehole ID	Easting	Northing	Sample type	Ore zone/ position in the mine	Intersection/ position (in meters)	Material analyzed
NS-01-SC	SC-10-006	509162.7	5179683.3	Black shale	Shale in the Newland Formation below MSZ	432.0	Black shale
NS-05-SC	SC-11-013	506745.4	5180829.6	Fine-grained pyrite with barite pseudomorphs	In barite zone, above Cu zone, within USZ	45.9	Pyrite
NS-17-SC	SC-10-006	509162.7	5179683.3	Fine-grained pyrite, the earliest pyrite generation	Between USZ and MSZ	324.0	Pyrite
NS-03-SC	SC-11-013	506745.4	5180829.6	Alternating layers of chalcopyrite with calcite	Cu zone within USZ	54.5	Chalcopyrite
NS-35-SC	SC-12-138	506620.2	5180343.4	Chalcopyrite+calcite+barite cementing very fine-grained pyrite clasts	In Cu zone within USZ	122.5–123.0	Chalcopyrite
NS-28-SC	SC-10-06	509162.7	5179683.3	Coarse-grained chalcopyrite in fine-grained pyrite and shale breccia clasts in debris flow	In MSZ	410.0	Chalcopyrite
NS-29-SC	SC-10-06	506745.4	5180829.6	Chalcopyrite stringers, no pyrite	In MSZ	419.0	Chalcopyrite
NS-24-SC	SC-12-100	507169.2	5180813.5	Coarse-grained chalcopyrite in calcite vein	In Cu zone in LSZ	416.0	Chalcopyrite
NS-25-SC	SC-12-100	507169.2	5180813.5	Coarse-grained chalcopyrite in calcite vein	In Cu zone in LSZ	422.0	Chalcopyrite

of each chalcopyrite mineral separate was embedded in epoxy to determine qualitatively the purity of the mineral separates. These mounts were studied by using a reflected light microscope.

3.3. Preparation of Sulfide Mineral Separates. All samples were cut into slabs that were thoroughly cleaned using silicon carbide grit, ultrapure (18.2 MΩ) water, and ethanol to remove any metal traces introduced by hammering or sawing. The shale sample was split into two aliquots that were powdered in an automated agate mill. All sulfide samples were crushed using a zirconia ceramic dish and puck and sieved through disposable, home-made nylon sieves to produce 70–200 and +70 mesh-size fractions. A Frantz Isodynamic Separator was used to produce magnetic (M) and nonmagnetic (NM) subfractions from the 70–200 mesh fractions by applying successive amp currents with 15° side slope and 10° forward slope (protocol adapted from [39]), as follows: (1) 0.3 and 0.6 amp currents were used to collect pyrite fractions from the pyrite-only samples and (2) a 1.3 amp current was used for the chalcopyrite-bearing samples from which chalcopyrite was collected in the M1.3 fraction. The sulfide species were then isolated from remaining gangue minerals into final sulfide mineral separates by heavy liquid separation using Sodium Polytungstate (SPT, specific gravity 2.86) with a minimum of ten rinses using ultrapure (18.2 MΩ) water, followed by a rinse with ethanol prior to dry down in an oven at 60°C overnight.

3.4. Re-Os Isotope Geochemistry. For each analysis, between 200 and 550 mg of sulfide (pyrite or chalcopyrite) mineral separate or shale powder was weighed and transferred into a thick-walled borosilicate Carius tube [42]. Each sulfide aliquot was dissolved in inverse Aqua Regia (~3 mL of 11 N HCl and ~6 mL of 16 N HNO_3), together with a known amount of ^{185} Re + ^{190}Os spike solution at 220°C for 24 hours. Each shale aliquot was dissolved in ~8 mL of a mixture of CrO_3–H_2SO_4 with a known amount of ^{185} Re + ^{190}Os spike solution at 220°C for 48 h (Canadian Centre for Isotopic Microanalysis, University of Alberta, Edmonton, Canada, and Laboratory for Sulfide and Source Rock Geochemistry and Geochronology, Durham University, Durham, UK). The Re-Os laboratory protocol used in the present work is described in full in Selby et al. [43] and Cumming et al. [44].

Rhenium and Os isotopic compositions were determined by negative thermal ionization mass spectrometry (N-TIMS) using a Thermo Scientific Triton mass spectrometer at the Canadian Centre for Isotopic Microanalysis, University of Alberta, Edmonton, Canada (pyrite and shale), and at the Arthur Holmes Laboratory, Durham University, Durham, UK (chalcopyrite). Rhenium was measured as ReO_4^- in static mode on Faraday collectors; Os was measured as OsO_3^- in peak-hopping mode on SEM with a constant flow of oxygen [45, 46]. Quality of the measurements of the Re and Os isotopic compositions of pyrite and shale was monitored by repeated analyses of in-house Re (^{185} Re/^{187} Re = 0.59774 ± 0.00065, n = 23) and Os ("AB-2," ^{187}Os/^{188}Os = 0.10682 ± 0.00009,

$n = 100$) standard solutions at the University of Alberta. Likewise, for chalcopyrite aliquots, repeated measurements of in-house Re (^{185} Re/^{187} Re = 0.59892 ± 0.00203, $n = 74$) and Os ("DROsS 4.5b," ^{187}Os/^{188}Os = 0.16087 ± 0.00041, $n = 100$) standard solutions were carried out at Durham University. Total procedural blanks for each set of samples are reported in Table 2. The presented uncertainties listed in Table 2 include propagated uncertainties in the standard, spike calibrations, mass spectrometry measurements, and blanks.

3.5. Sulfur Isotopic Composition of the Chalcopyrite Mineral Separates. About 5 to 10 mg of chalcopyrite mineral separate was utilized for each sulfur isotopic analysis. Sulfides were analyzed by standard techniques [47] in which SO_2 gas was liberated by combusting the sulfides with excess Cu_2O at 1,075°C, in vacuo, at the Scottish Universities Environmental Research Centre (SUERC), Glasgow, UK. The liberated gases were analyzed on a VG Isotech SIRA II mass spectrometer, and standard corrections were applied to raw $\delta^{66}SO_2$ values to produce true $\delta^{34}S$. Standards employed were the international standards NBS-123 and IAEA-S-3 and the SUERC standard CP-1. Repeat analyses of these standards gave $\delta^{34}S$ values of +17.1‰, −32.0‰, and −4.6‰, respectively, with a standard error of ±0.3‰. Data are reported in conventional $\delta^{34}S$ notation as per mil (‰) variations from the Vienna Cañon Diablo Troilite (VCDT) standard.

3.6. Finite Mixture Modeling of Re-Os Data and Isochron Regression. To statistically assess whether the data may belong to multiple regression lines, we iteratively fit a series of finite mixture models to the data, where each finite mixture represents a linear regression with an intercept and slope (i.e., a potential isochron) [48]. We test whether the maximum number of mixture components can lie between 1 and 5 (i.e., 1 to 5 potential and discrete regression lines) and compare the results using a model comparison score to choose the best-fitting model (Integrated Completed Likelihood Criterion, ICL parameter). We utilize the ^{187}Re/^{188}Os and ^{187}Os/^{188}Os ratios and the error correlation factor *rho* for each data point. Those parameters are conventionally used to plot Re-Os data in the ^{187}Os/^{188}Os vs. ^{187}Re/^{188}Os space as error ellipses. In the present modeling exercise, we represent each data point of a sulfide aliquot using 100 points to account for the elliptical uncertainty in the ^{187}Re/^{188}Os and ^{187}Os/^{188}Os ratios (Figures 3(a) and 4(a)), but assume that all 100 points belong to a single aliquot and its uncertainty ellipse must belong to the same isochron.

In detail, we run the R script provided by Davies et al. [48], which utilizes the *Flexmix* package [49]. All text in quotation marks that follows represents inputs into the R script [48]. We run the model with 100 points for each sulfide aliquot, to capture the analytical uncertainty in each measurement, but assume that all 100 points belong to a single aliquot and therefore the same isochron. Hence, we set the parameters "iterate = 50" and "random.effects = TRUE". We test for the possibility that the data can be explained by up to five possible isochrons, using the expectation-maximization (EM) algorithm in the Flexmix package. We allow up to 1,000 possible iterations of the EM algorithm to allow it to converge ("n.iter = 1,000"). In our case, all runs for of the EM algorithm converged (Tables 1 and 2). To account for variability in the initiation of the EM algorithm, we repeated 100 times the search for 1 to 5 components ("n.rep = 100").

We used Isoplot v. 4.15 [50] to report all Re-Os dates as Model 1 or Model 3 isochrons through statistical regression of the Re-Os data, which are reported at the 2σ level (95% level of confidence), in the ^{187}Os/^{188}Os vs. ^{187}Re/^{188}Os space using the decay constant of ^{187}Re (λ^{187} Re = $1.666e^{-11} \pm 5.165e^{-14}$ a^{-1}) [51]. Error propagation was also investigated using the Monte Carlo approach [52]. In this technique, a prescribed number of isochrons are constructed from the input data and their corresponding probability density function (analytical uncertainty of the ^{187}Re/^{188}Os and ^{187}Os/^{188}Os ratios and their error correlation *rho*). The Re-Os date and estimate of the initial ^{187}Os/^{188}Os ratio are cross-plotted yielding a probabilistic distribution that includes an analytical uncertainty. Given the use of error propagation *rho*, the analytical uncertainty presented above inherently includes both random and systematic uncertainties. Further, model uncertainties include the assumptions that all samples have nearly identical ages and the same initial ^{187}Os/^{188}Os composition, and for those aliquots, the Re-Os system remained closed.

4. Results

4.1. Petrography of Chalcopyrite Mineralization and Mineral Separates. Five styles of copper mineralization were studied (Figures 2(b) and 2(c)): (i) stratiform and varve-like chalcopyrite (sample 03-SC) associated with, and replacing, massive pyrite in the Upper Sulfide Zone (samples 05-SC and 17-SC); (ii) chalcopyrite replacing pyrite and barite in a barite ± quartz-cemented, pyrite-walled tube structure (as described by [6]; sample 35-SC); (iii) discordant, stringer-type chalcopyrite in the Middle Sulfide Zone (sample 29-SC); (iv) chalcopyrite cement in polymictic shale and a massive pyrite debris flow (sample 28-SC); and (v) coarse-grained chalcopyrite in calcite veins (samples 24-SC and 25-SC). Chalcopyrite in all styles of mineralization lacks any obvious sign of recrystallization (Figure 2(c)).

4.2. Re-Os Isotope Geochemistry of Black Shale, Pyrite, and Chalcopyrite. The two black shale aliquots have Re and total Os contents of 11.8 to 13.3 ppb and 285 to 324 ppt, respectively (Table 2). Common Os, for which the best approximation is given by contents in ^{192}Os, represents ca. 14% of total Os contents. The Os budget in these shale aliquots is thus dominated by radiogenic ^{187}Os. These shale aliquots have relatively similar ^{187}Re/^{188}Os values (567–588) and highly radiogenic (14.5–15.0) ^{187}Os/^{188}Os ratios. For a depositional age in excess of 1,475 Ma for the Newland Formation, the calculated range of initial ^{187}Os/^{188}Os ratios (Os_i) for those aliquots is 0.342 ± 0.004 and 0.354 ± 0.003. These Os_i values must be positive and greater than the value of the ^{187}Os/^{188}Os ratio for the mantle in that age range ($Os_{mantle\,1,475\,Ma}$ = 0.12 ± 0.02, calculated for the hypothetical primitive Mesoproterozoic upper mantle at 1,475 Ma by using present-day

Table 2: (a) Re-Os isotope geochemistry data for chalcopyrite, pyrite and black shale aliquots. (b) Blank compositions for each aliquot type are given. Abbreviations: n.a.: not analyzed; Os_i: initial $^{187}Os/^{188}Os$ ratio of a given aliquot at a given date.

(a)

Aliquot type	$\delta^{34}S$ (±0.3‰-VDCT)	Magnetic fraction	Mineralization style	Mineralized zone	Weight (mg)	Re (ppb)	±2σ	Os (ppt)	±2σ	^{192}Os (ppt)	$^{187}Re/^{188}Os$	±2σ	$^{187}Os/^{188}Os$	±2σ	*Rho*	%Re blank	$\%^{187}Os$ blank	$\%^{188}Os$ blank	Cluster number in Figures 3 and 4
Chalcopyrite	−2.3	03-SC M1.3	Stratiform	USZ	389.44	0.459	0.006	49.6	0.3	17.9	51	1	1.24	0.01	0.434	1.34	0.12	0.58	1
Chalcopyrite	−2.3	03-SC M1.3	Stratiform	USZ	381.20	0.351	0.002	22.9	0.1	7.2	97	1	2.52	0.03	0.682	1.72	0.35	1.09	3
Chalcopyrite	−2.3	03-SC M1.3	Stratiform	USZ	382.23	0.458	0.002	12.5	0.2	2.3	401	9	9.84	0.25	0.803	1.31	0.28	3.38	1
Chalcopyrite	−2.3	35-SC M1.3	Stratiform	USZ	402.73	0.747	0.003	20.7	0.3	3.7	402	6	10.20	0.18	0.747	0.76	0.16	2.00	3
Chalcopyrite	+1.9	28-SC M1.3	Stringer-type	MSZ	387.48	1.223	0.006	41.0	0.4	9.9	247	3	5.66	0.07	0.852	0.51	0.05	1.05	2
Chalcopyrite	+1.9	28-SC M1.3	Stringer-type	MSZ	396.43	0.821	0.005	29.2	0.3	7.2	226	4	5.26	0.08	0.868	0.74	0.07	1.40	2
Chalcopyrite	+2.1	29-SC M1.3	Stringer-type	MSZ	400.07	0.914	0.006	40.4	0.4	10.6	171	2	4.48	0.05	0.785	0.66	0.05	0.94	3
Chalcopyrite	−2.5	25-SC M1.3	Chalcopyrite in calcite veins	LSZ	317.70	0.404	0.006	23.6	0.3	7.3	110	3	2.70	0.06	0.701	1.87	0.16	1.73	1
Chalcopyrite	−2.5	25-SC M1.3	Chalcopyrite in calcite veins	LSZ	387.64	0.424	0.002	1079.8	3.1	442.8	1.91	0.01	0.18	0.00	0.595	1.40	0.08	0.02	3
Chalcopyrite	−2.5	25-SC M1.3	Chalcopyrite in calcite veins	LSZ	300.30	0.487	0.007	28.0	0.4	8.6	113	3	2.78	0.06	0.670	1.64	0.14	1.56	1
Chalcopyrite	−4.1	24-SC M1.3	Chalcopyrite in calcite veins	LSZ	359.09	0.725	0.003	42.7	0.2	12.6	115	1	3.22	0.03	0.641	0.88	0.17	0.67	2
Chalcopyrite	−4.1	24-SC M1.3	Chalcopyrite in calcite veins	LSZ	365.98	0.698	0.003	35.9	0.2	9.9	140	1	3.89	0.03	0.680	0.90	0.17	0.83	2
Pyrite	n.a.	05-SC M0.3	Massive pyrite	USZ	488.73	1.034	0.004	25.6	0.3	4.5	453	5	10.29	0.20	0.549	0.46	0.11	1.37	2
Pyrite	n.a.	05-SC M0.3	Massive pyrite	USZ	405.73	0.946	0.004	24.5	0.6	4.1	456	13	11.22	0.33	0.980	0.17	0.22	8.94	3
Pyrite	n.a.	05-SC M0.3	Massive pyrite	USZ	192.95	0.928	0.004	22.8	1.5	3.6	514	36	12.57	0.89	0.996	0.37	0.48	21.59	3
Pyrite	n.a.	05-SC M0.6	Massive pyrite	USZ	431.12	0.859	0.004	22.3	0.2	4.0	425	4	10.05	0.10	0.855	0.62	0.14	1.75	2
Pyrite	n.a.	05-SC M0.6	Massive pyrite	USZ	404.41	0.754	0.003	20.4	0.6	3.5	433	15	11.06	0.39	0.986	0.22	0.27	10.69	1
Pyrite	n.a.	05-SC M0.6	Massive pyrite	USZ	400.89	0.743	0.003	20.4	0.6	3.6	414	15	10.51	0.38	0.949	0.22	0.28	10.45	1

Table 2: Continued.

Aliquot type	$\delta^{34}S$ (±0.3‰-VDCT)	Magnetic fraction	Mineralization style	Mineralized zone	Weight (mg)	Re (ppb)	±2σ	Os (ppt)	±2σ	^{192}Os (ppt)	$^{187}Re/^{188}Os$	±2σ	$^{187}Os/^{188}Os$	±2σ	*Rho*	%Re blank	$\%^{187}Os$ blank	$\%^{188}Os$ blank	Cluster number in Figures 3 and 4
Pyrite	n.a.	05-SC M0.6	Massive pyrite	USZ	468.81	0.647	0.003	16.0	0.2	2.7	469	6	10.98	0.14	0.899	0.76	0.17	2.36	2
Pyrite	n.a.	05-SC NM0.6	Massive pyrite	USZ	410.98	0.587	0.002	14.8	0.7	2.4	496	25	12.35	0.63	0.985	0.28	0.35	15.48	1
Pyrite	n.a.	05-SC NM0.6	Massive pyrite	USZ	406.90	0.590	0.003	14.8	0.7	2.3	502	15	12.51	0.66	0.983	0.28	0.35	15.74	1
Pyrite	n.a.	17-SC-3 NM0.3	Massive pyrite	USZ	551.91	1.295	0.005	40.1	0.2	8.1	318	2	8.10	0.05	0.529	0.32	0.07	0.68	3
Pyrite	n.a.	17-SC-3 NM0.3	Massive pyrite	USZ	469.56	1.302	0.005	40.2	0.1	8.1	318	2	8.07	0.04	0.636	0.38	0.08	0.79	3
Shale	n.a.	01-SC-A	—	Below MSZ	282.89	11.840	0.043	285	2.8	40.1	588	5	14.97	0.13	0.834	0.40	0.01	0.93	—
Shale	n.a.	01-SC-B	—	Below MSZ	280.18	13.270	0.046	324	2.9	46.6	567	4	14.46	0.10	0.832	0.36	0.01	0.95	—

(b)

Blank type	Type of material analyzed	Blanks Os (ppt)	Blanks ±2σ	$^{187}Os/^{188}Os$	±2σ	Re (ppt)	±2σ
Aqua Regia	Chalcopyrite	0.57	0.02	0.21	0.06	7.7	1.3
Aqua Regia	Chalcopyrite	0.08	0.02	0.80	0.06	2.3	0.2
CrO_3-H_2SO_4	Shale	0.30	0.10	0.20	0.05	15.0	3.0
Aqua Regia	Pyrite	0.08	0.02	0.80	0.06	2.3	0.2

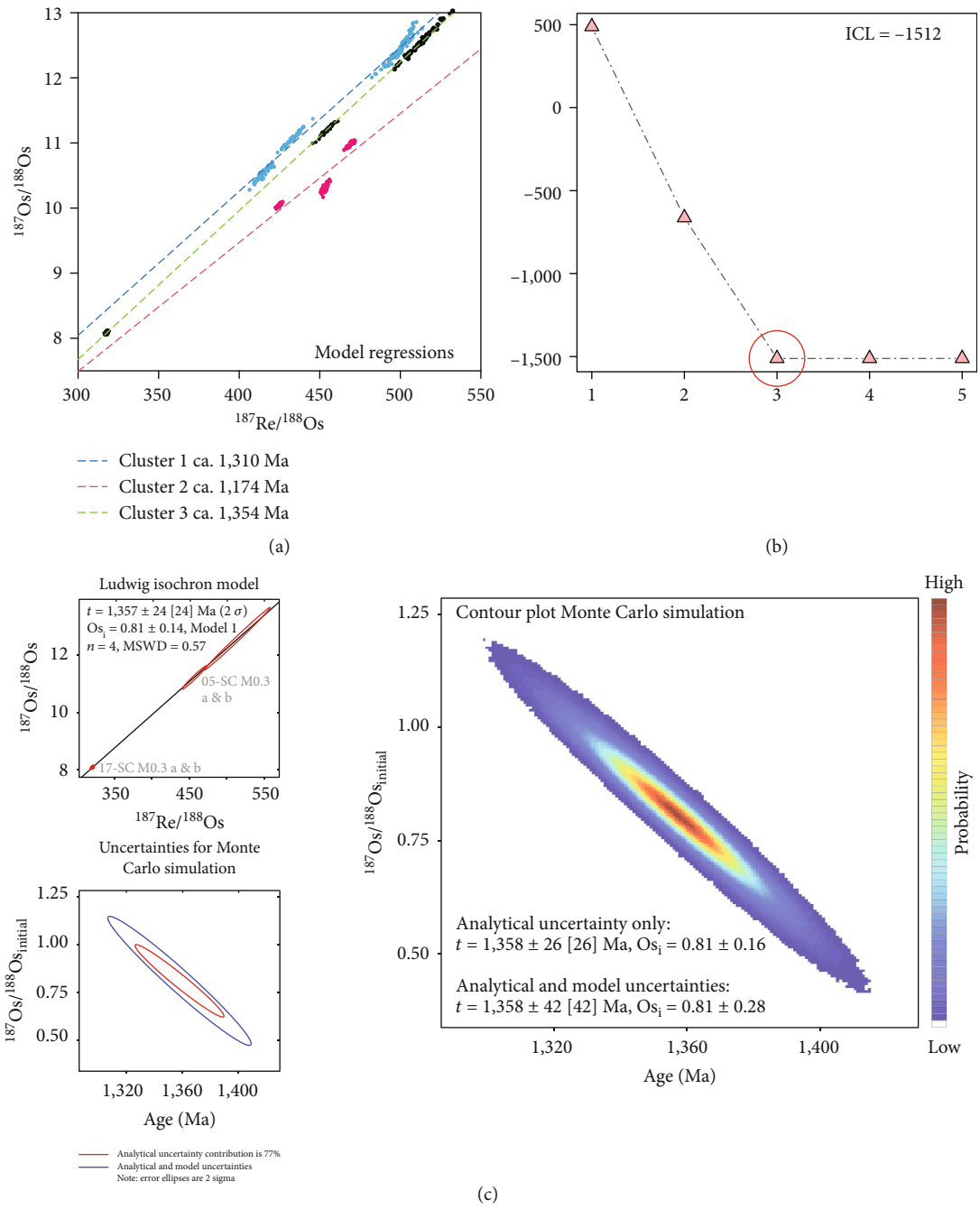

Figure 3: (a) Modeled isochrons plotted through the clusters suggested by the model for Re-Os data of pyrite. Each isochron is colored differently. (b) Optimum number of mixture components for different numbers using the Integrated Completed Likelihood Criterion (ICL parameter). (c) Re-Os isochron model and Monte Carlo simulation for pyrite data in "cluster 3." Individual ellipses show 2σ uncertainty of each data point in $^{187}Os/^{188}Os$ vs. $^{187}Re/^{188}Os$ space. Ellipses are constructed from maximum and minimum error vectors that are orthogonal to each other. Maximum and minimum uncertainties are statistical values that are calculated from uncertainty of the $^{187}Os/^{188}Os$ and $^{187}Re/^{188}Os$ ratios for a given data point. Final uncertainties were calculated by full error propagation of uncertainties in the Re and Os measurements, blank values, isotopic compositions, spike calibrations, and reproducibility of the standard Re and Os values. Error correlation function, rho, is utilized for isochron regressions [50]. Isochron uncertainty does not include uncertainty in the ^{187}Re decay constant [50, 51].

values of $^{187}Re/^{188}Os = 0.435 \pm 0.055$ and $^{187}Os/^{188}Os = 0.130 \pm 0.001$ for the primitive upper mantle) [53, 54].

The fine-grained, sedimentary massive pyrite has Re and total Os contents of 0.59 to 1.30 ppb and 14.8 to 40.2 ppt, respectively. Common Os is approximately ca. 16 to 20% of the total Os content, which is largely dominated by radiogenic ^{187}Os (Table 2). The $^{187}Re/^{188}Os$ and $^{187}Os/^{188}Os$ values range from 318 to 514 and 8.1 to 12.6, respectively.

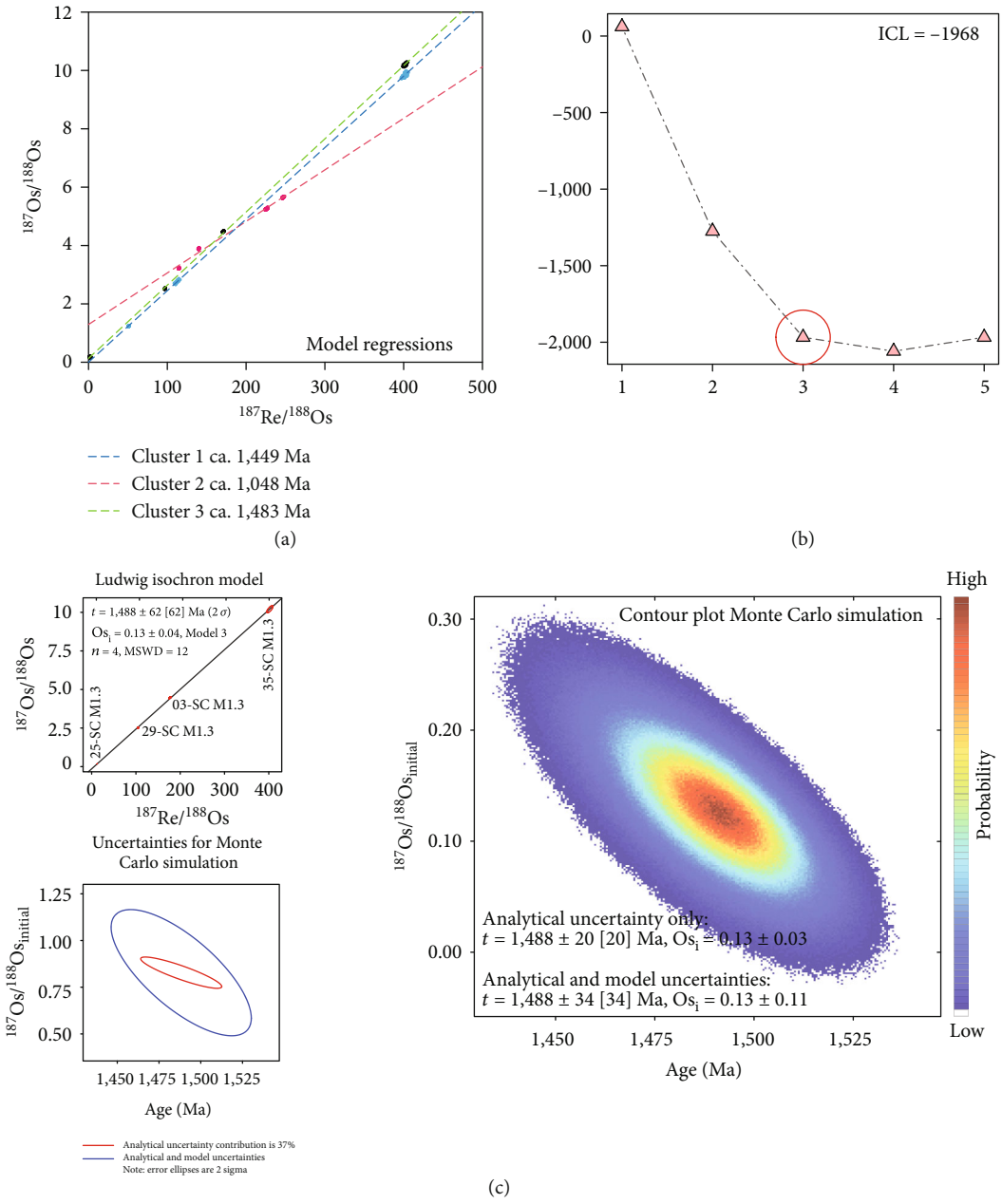

FIGURE 4: (a) Modeled isochrons plotted through the clusters suggested by the model for Re-Os data of chalcopyrite. Each isochron is colored differently. (b) Optimum number of mixture components for different numbers using the Integrated Completed Likelihood Criterion (ICL parameter). (c) Re-Os isochron model and Monte Carlo simulation for chalcopyrite data in "cluster 3." Individual ellipses show 2σ uncertainty of each data point in $^{187}Os/^{188}Os$ vs. $^{187}Re/^{188}Os$ space. Ellipses are constructed from maximum and minimum error vectors that are orthogonal to each other. Maximum and minimum uncertainties are statistical values that are calculated from uncertainty of the $^{187}Os/^{188}Os$ and $^{187}Re/^{188}Os$ ratios for a given data point. Final uncertainties were calculated by full error propagation of uncertainties in the Re and Os measurements, blank values, isotopic compositions, spike calibrations, and reproducibility of the standard Re and Os values. Error correlation function, rho, is utilized for isochron regressions [50]. Isochron uncertainty does not include uncertainty in the ^{187}Re decay constant [50, 51].

The eleven aliquots of pyrite yield a Model 3 regression with a Re-Os date of 1,156 ± 46 Ma, 2σ, and $Os_i = 1.94 \pm 1.08$ (Mean Square Weighted Deviates (MSWD) = 59).

Rhenium and total Os contents in the twelve chalcopyrite aliquots are 0.35 to 1.22 ppb and 12.5 to 1,080 ppt, respectively (Table 2). Common Os represents ca. 18 to 41% of the total Os contents that are dominated by radiogenic ^{187}Os. These chalcopyrite aliquots have moderate and variable $^{187}Re/^{188}Os$ ratios (51–401) and variably radiogenic $^{187}Os/^{188}Os$ compositions (1.24–10.20). The twelve aliquots of chalcopyrite yield a Model 3 regression with a Re-Os date of 1,455 ± 24 Ma, 2σ, and $Os_i = 0.13 \pm 0.03$ (MSWD = 68).

Table 3: Summary table for one to five mixture components used to fit to the pyrite Re-Os data.

Maximum mixture components	Iterations	Converged	k	k_0	logLik	AIC	BIC	ICL
1	1,000	True	1	1	-234.7	475.4	488.3	488.3
2	1,000	True	2	2	353.6	-693.3	-663.1	-663.1
3	1,000	True	3	3	790.5	-1,559.1	-1,511.6	-1,511.6
4	999	True	3	4	790.5	-1,559.1	-1,511.6	-1,511.6
5	999	True	3	5	790.5	-1,559.1	-1,511.6	-1,511.6

Table 4: Summary table for one to five mixture components used to fit to the chalcopyrite Re-Os data.

Maximum mixture components	Iterations	Converged	k	k_0	logLik	AIC	BIC	ICL
1	1,000	True	1	1	-20.7	47.5	60.7	60.7
2	1,000	True	2	2	659.8	-1,305.7	-1,274.9	-1,274.9
3	1,000	True	3	3	1,019	-2,016	-1,967.6	-1,967.6
4	999	True	3	4	1,064.6	-2,107.1	-2,058.8	-2,058.8
5	999	True	3	5	1,019	-2,016	-1,967.6	-1,967.6

4.3. Sulfur Isotopic Composition of Chalcopyrite Mineral Separates. The various styles of chalcopyrite mineralization have discrete sulfur isotopic signatures (Table 2). Stratiform, varve-like chalcopyrite in the Upper Sulfide Zone (sample 03-SC) has a δ^{34}S value of –2.3‰. Chalcopyrite that replaces the pyrite-walled, barite-cemented tube structures (sample 35-SC) has an identical value. The sulfur isotopic composition of coarse-grained chalcopyrite in calcite veins within the Lower Sulfide Zone (samples 24-SC and 25-SC) shows a range of –4.1 to –2.5‰. In contrast, chalcopyrite that replaces a debris flow (sample 28-SC) and occurs in discordant, stringer-type mineralization (sample 29-SC) in the Middle Sulfide Zone has δ^{34}S values of +1.9‰ and+2.1‰, respectively.

5. Discussion

5.1. Evaluation of Re-Os Dates and Timing of Pyrite and Chalcopyrite Mineralization. The Model 3 apparent "isochrons" for pyrite and chalcopyrite have very high MSWD ($MSWD_{pyrite} = 59$ and $MSWD_{chalcopyrite} = 68$) with dates and initial $^{187}Os/^{188}Os$ ratios of unknown geological integrity. These apparent "isochrons" are interpreted as resulting from an excess scatter around a regression line because several aliquots may not have had closed Re-Os systematics since the time of sulfide precipitation. Such excess scatter could be related to partial resetting of several aliquots or to multiple time components in a dataset that record discrete geological processes in time and/or initial $^{187}Os/^{188}Os$ isotopic composition [48, 55].

In the following, we remediate this situation by deciphering and weighing against independent geological evidence, the three mixture components identified for both pyrite and chalcopyrite using the Integrated Completed Likelihood Criterion (ICL criterion) and the cluster analysis (pyrite: Figures 3(a) and 3(b); chalcopyrite: Figures 4(a) and 4(b)). We treat here data for pyrite and chalcopyrite separately. To choose the optimum number of potential mixture components, we compared the results for different numbers using the ICL criterion. The larger the negative value of the ICL parameter, the better the model statistically describes the data. We plot the ICL parameter for both the pyrite and chalcopyrite data separately (Figures 3(b) and 4(b)). In both cases, it can be seen that the ICL and the other model fitting parameters (i.e., logLik, AIC, BIC) ([48]; Tables 3 and 4) collectively suggest three mixture components to describe the pyrite and chalcopyrite data, respectively. For the pyrite data, the lowest ICL value is found so that a model of 3 mixture components would sufficiently describe the data (Figure 3(b) and Table 3). In the case of the chalcopyrite data, we choose 3 mixture components, even though 4 provide a slightly lower ICL value. This is because the model for 4 components actually converged to 3 components (Figure 4(b) and Table 4).

5.1.1. Pyrite. In light of the ICL criterion and cluster analysis, finite mixture modeling identified three discrete components for the Re-Os data of pyrite (Figures 3(a) and 3(b)). For each data cluster, a gross Re-Os date estimate is based on linear regression of the number of data points (n) belonging to each cluster (Figure 3(a)). Those estimates range from 1,354 Ma (cluster 3, $n = 4$, 36.4% of the data, samples py-05 and py-17, modeled $Os_i = 0.82$), 1,310 Ma (cluster 1, $n = 4$, 36.4% of the data, sample py-05, modeled $Os_i = 1.41$), and 1,174 Ma (cluster 2, $n = 3$, 27.2% of the data, sample py-05, modeled $Os_i = 1.55$). None of those gross date estimates coincide with the age of deposition of the Newland Formation at ca. >1,475 Ma comprising fine-grained sediments and associated synsedimentary to diagenetic pyrite. To interpret these results, we computed Re-Os isochron dates for clusters with at least four defining data points using Isoplot v.4.15 [50] and the Monte Carlo simulation-based application [52].

For "cluster 3," the data define a Model 1 Re-Os isochron date of 1,357 ± 24 [24] Ma (2σ, $n = 4$, MSWD = 0.57, $Os_i = 0.81 \pm 0.14$, with $[x]$ including the uncertainty on the decay constant of ^{187}Re as determined by [51]; Figure 3(c)). The Monte Carlo simulation returns a Re-Os isochron date of

1,358 ± 42 [42] Ma with an Os_i of 0.81 ± 0.28 (2σ, where [y] represents the analytical and model uncertainties, including 77% contributed by analytical uncertainties only). For "cluster 1," a Model 1 Re-Os isochron date of 1,280 ± 117 [118] Ma (2σ, n = 4, MSWD = 1.7, Os_i = 1.67 ± 0.86, with [x] including the uncertainty on the decay constant of ^{187}Re as determined by [51]; Supplementary Figure 1). The Monte Carlo simulation returns a Re-Os isochron date of 1,312 ± 289 [289] Ma with an Os_i of 1.41 ± 2.24 (2σ, where [y] represents the analytical and model uncertainties, including 76% contributed by analytical uncertainties only). In "cluster 1," the high uncertainty in the modeled Re-Os isochron dates is related to the limited range of spread of ^{187}Re/^{187}Os values of the analyzed aliquots (i.e., [400; 550]). The Re-Os date of ca. 1,358 Ma ("cluster 3") and the tentative Re-Os date of ca. 1,312 Ma ("cluster 1") overlap within uncertainty with the timing of the East Kootenay orogeny between ca. 1,379 and 1,325 Ma [56–58] during which thermal events could have reset the Re-Os systematics of synsedimentary to diagenetic pyrite. Indeed, magmatic-hydrothermal activity in the Belt-Purcell Basin was identified between ca. 1,383 and 1,325 Ma in connection with intrusion of a suite of gabbro-granite plutons between ca. 1,383 and 1,359 Ma [17, 19, 59]. This particular magmatic-hydrothermal event is known to have triggered cobalt and rare earth mineralization in the Idaho cobalt belt in the Belt-Purcell Basin ([60]; ca. 1,349 Ma Re-Os isochron age of cobaltite, [39]; Figure 1).

The gross Re-Os estimate defined by three data points in "cluster 2" at ca. 1,174 Ma is inconclusive. This date might be a pseudoisochron age. Therefore, more work is warranted to investigate if this date could be related to a partial resetting of Re-Os systematics in pyrite (e.g., [55]) caused by thermal events during the Grenvillian orogeny recognized worldwide between ca. 1,190 and 1,006 Ma [17, 39, 41, 56, 58, 61, 62]. This Grenvillian event, which has been recently confirmed to have impacted geological units located in northwestern present-day North America, was responsible for widespread hydrothermal activity causing mineral precipitation (or recrystallization) in the Belt-Purcell Basin between ca. 1,160 and 1,040 Ma [21, 39, 59, 63].

In conclusion, we infer that thermal events associated with the East Kootenay orogeny may have impacted and caused partial resetting of Re-Os systematics in synsedimentary to diagenetic pyrite with an assumed age equivalent to the depositional age of the Newland Formation. Due to tectonic and thermal events that partially reset the Re-Os clock in discrete pyrite samples, the initial ^{187}Os/^{188}Os ratio in pyrite increased from an unknown value at the time of synsedimentary to diagenetic pyrite mineralization at ca. >1,475 Ma to 0.81 ± 0.28 at ca. 1,358 Ma. This evolution of initial ^{187}Os/^{188}Os ratios identifies a crustal contribution in radiogenic ^{187}Os during the East Kootenay orogenic episode and associated (magmatic-)hydrothermal events affecting the Re-Os systematics of an original synsedimentary to diagenetic pyrite.

5.1.2. Chalcopyrite. In light of the ICL criterion and cluster analysis, finite mixture modeling for Re-Os data of chalcopyrite identified three discrete components (Figures 4(a) and 4(b)). The gross Re-Os date estimates are based on linear regressions of an even number of aliquots (n = 4, 33.3% of the data in each cluster): ca. 1,483 Ma for "cluster 3" (samples cpy-03, cpy-25, cpy-29, and cpy-35, modeled Os_i = 0.13); ca. 1,449 Ma for "cluster 1" (samples cpy-03 and cpy-25, modeled Os_i = 0.00); and ca. 1,048 Ma for "cluster 2" (samples cpy-24 and cpy-28, modeled Os_i = 1.29). As done for pyrite, we computed Re-Os isochron dates for clusters with at least four defining data points using Isoplot v. 4.15 [50] and the Monte Carlo simulation-based [52].

Data in "cluster 3" yield a Model 3 isochron with a Re-Os date of 1,488 ± 62 [62] Ma, (2σ, MSWD = 12) and an initial ^{187}Os/^{188}Os ratio of 0.13 ± 0.04 (Figure 4(c)). The Monte Carlo simulation of this same data cluster shows that the analytical and model uncertainties contribute to 37% and 63% of the total uncertainty, respectively. This Monte Carlo simulation yields a Re-Os date of 1,488 ± 34 [34] Ma and an initial ^{187}Os/^{188}Os ratio of 0.13 ± 0.11. This Re-Os date of 1,488 ± 34 [34] Ma overlaps with the geological age of the Newland Formation at ca. >1,475 Ma. Hence, we interpret that chalcopyrite mineralization was potentially contemporaneous (within uncertainty) with sedimentation and diagenesis of the Newland Formation. This interpretation is compatible with independent conclusions proposing a diagenetic origin for chalcopyrite mineralization [7] and its connection with magmatic-hydrothermal activity at and below the sediment-water interface [6].

The regression of data belonging to "clusters 1 and 2" indicates possible disturbance of these samples following the initial closure of the Re-Os isotopic system. Data in "cluster 1" yield a Model 1 isochron with a Re-Os date of 1,460 ± 79 [80] Ma (2σ, MSWD = 0.02) with a geologically unrealistic initial ^{187}Os/^{188}Os ratio of –0.01 ± 0.10 and a Monte Carlo simulation with Re-Os date of 1,454 ± 113 [113] Ma and an initial ^{187}Os/^{188}Os ratio of 0.00 ± 0.29 (Supplementary Figure 2). We interpret those unrealistic date and Os_ias resulting from a limited disturbance of the Re-Os systematics in the samples belonging to "cluster 1." Data in "cluster 2" define a Model 3 isochron with a highly imprecise Re-Os date of 1,055 ± 264 [264] Ma (2σ, MSWD = 102) with an initial ^{187}Os/^{188}Os ratio of 1.29 ± 0.85 and a Monte Carlo simulation with Re-Os date of 1,052 ± 165 [165] Ma and an initial ^{187}Os/^{188}Os ratio of 1.28 ± 0.53 (Supplementary Figure 3). The results of this regression are inconclusive and result from the limited spread of ^{187}Re/^{188}Os values over which the isochron was modeled.

5.2. Sources of Osmium and Reduced Sulfur in Copper Mineralization. The initial ^{187}Os/^{188}Os isotopic composition of sulfides may be utilized to trace the source of Os and by inference other metals (e.g., Cu), from potential source(s) [64, 65]. This evaluation is possible for a Re-Os dataset with limited scatter and uncertainty of the initial ^{187}Os/^{188}Os isotopic composition, e.g., the Os_i value of 0.13 ± 0.11 for the ca. 1,488 Ma Re-Os isochron age for synsedimentary to diagenetic chalcopyrite mineralization determined in this study.

The best representation of the ^{187}Os/^{188}Os isotopic composition of the upper continental crust at the time of

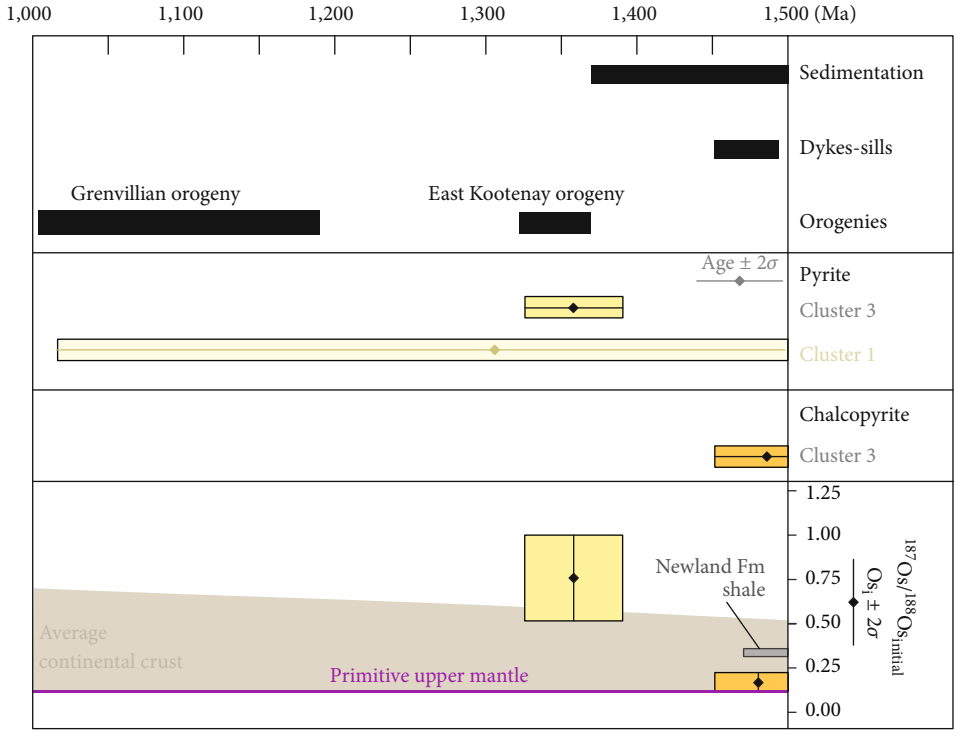

FIGURE 5: Synopsis of geological processes and orogenies vs. identified base metal mineralizing events in the Helena Embayment between 1,500 and 1,000 Ma (see text for details and references). The initial $^{187}Os/^{188}Os$ isotopic composition (Os_i) of the dated chalcopyrite (orange) and pyrite (yellow) in this study is compared to the $^{187}Os/^{188}Os$ isotopic composition of potential reservoirs in the study area at the time of mineralization (i.e., chalcopyrite) or reset of the ^{187}Re-^{187}Os chronometer (i.e., pyrite). The $^{187}Os/^{188}Os$ isotopic composition for an average continental crust is modeled after Chen et al. [66]. The $^{187}Os/^{188}Os$ isotopic composition for the primitive upper mantle is modeled after Meisel et al. [54] and Carlson [53].

chalcopyrite mineralization in the area of Black Butte is given by (1) the initial $^{187}Os/^{188}Os$ isotopic composition (0.34–0.35) of the black shale in the ca. >1,475 Newland Formation determined in the present study and (2) the estimated $^{187}Os/^{188}Os$ ratio (0.30 ± 0.23) for the upper continental crust, independently calculated at ca. >1,475 Ma by using estimates of present-day $^{187}Re/^{188}Os$ and $^{187}Os/^{188}Os$ ratios of 20 ± 12 and 0.80 ± 0.38, respectively, for the upper continental crust ([66]; Figure 5). In the Mesoproterozoic, the local upper continental crust in the Helena Embayment was a complex lithological collage comprising:

(i) the immediate basement to the Newland Formation including 500 to 1,000 m of unevenly laminated, interbedded black shale, siltstone, and sandstone of the Mesoproterozoic Chamberlain Formation and quartzite of the Mesoproterozoic Neihart Formation [67, 68], the latter unconformably overlying the 1.86 Ga Paleoproterozoic basement of the Great Falls Tectonic Zone (GFTZ; [69–75])

(ii) the NE-SW-trending GFTZ, which is a tectonic lineament that separates the 3.6 to 2.5 Ga Wyoming Craton to the southeast from the mixed Archean (3.6–2.5 Ga) and Paleoproterozoic (ca. 1.8 Ga) Medicine Hat Craton to the northwest [7, 70]. In situ laser ablation inductively coupled mass spectrometry U-Pb ages of zircon in gneiss and amphibolite have identified the presence of 3.2 to 2.4 Ga Archean protoliths that were involved in tectono-metamorphic processes at ca. 1.86 Ga and ca. 1.78 Ga within the GFTZ [70]. At ca. 1.8 Ga, in connection with creation of the GFTZ, this Proterozoic event involved fluid/melt that raised the Re/Os ratio of the subcontinental lithospheric mantle [76]. As such, the long-lived Paleoproterozoic and Archean basement of the GFTZ likely comprises lithologies having high Re/Os ratios. This interpretation is compatible with a lead component that was uniquely identified in barren and mineralized sedimentary belt rocks in the tectonically controlled Helena Embayment. Lead was there derived from the early Archean continental crust in the adjacent Wyoming Craton [77].

Considering as a lower limit the $^{187}Os/^{188}Os$ isotopic composition of the primitive Mesoproterozoic upper mantle at ca. >1,475 Ma ($Os_{mantle\ 1,475=}\ 0.12 \pm 0.02$), the Os_i value of 0.13 ± 0.11 for the ca. 1,488 Ma Re-Os isochron age for syn-sedimentary to diagenetic chalcopyrite mineralization defines a range of possible initial $^{187}Os/^{188}Os$ ratios for chalcopyrite from 0.10 to 0.24 (Figure 5). This range of initial $^{187}Os/^{188}Os$ ratios for chalcopyrite does not overlap with either the radiogenic initial $^{187}Os/^{188}Os$ isotopic composition (0.34–0.35) of black shale in the Newland Formation or the

interpreted higher range of radiogenic $^{187}Os/^{188}Os$ ratios (0.30–0.53) for the local upper continental crust calculated at ca. >1,475 Ma (Figure 5). In conclusion, the range of potential initial $^{187}Os/^{188}Os$ ratios for chalcopyrite from 0.11 to 0.24 is compatible with (1) a derivation of Os from a markedly unradiogenic magmatic source with a $^{187}Os/^{188}Os$ isotopic composition inherited from the upper mantle in the Mesoproterozoic ($Os_{mantle\ 1,475=}$ 0.12 ± 0.02) and (2) limited contamination in radiogenic ^{187}Os from a continental crustal source with an estimated $^{187}Os/^{188}Os$ isotopic composition of 0.30 ± 0.23 that could cause an increase of initial $^{187}Os/^{188}Os$ ratios for chalcopyrite up to 0.24.

In light of (1) our petrographic observations, (2) the unradiogenic, dominantly mantle-derived to low radiogenic source of Os in synsedimentary to early diagenetic Cu mineralization, and (3) considering that Cu mineralization occurred in the subsurface during continuous basin development and burial of the hydrothermal vents ([6]; this study), a magmatic source of sulfur could be permitted for chalcopyrite mineralization. Indeed, Lyons et al. [9] suggested that a narrow range of $\delta^{34}S$ signatures clustering around 0‰ in chalcopyrite may be indicative of a magmatic source of sulfur. Pyrite originally precipitated at the site of hydrothermal vents when metals titrated reduced sulfur produced by the metabolism of microorganisms in the water column with large sulfur isotopic fractionation (in excess of 50‰) in the immediate vicinity of metalliferous hydrothermal seepages [6]. Then, in the subsurface, thermal reduction of sulfate in barite contributed H_2S for base metal sulfide precipitation that was 10 to 20‰ lighter than seawater-derived sulfate in barite [6]. The bulk sulfur isotopic signature of chalcopyrite (–2.3‰, Table 2, this study), which replaced barite in sedimentary pyrite-walled tube structures (sample 35-SC), is compatible with this interpretation by Present et al. [6]. Yet, in all other samples analyzed in the present study, i.e., stringer-type, vein-type, varve-like chalcopyrite (Figure 2), in which barite is absent, it is possible that the sulfur was there predominantly of magmatic origin (–4.1 to +2.1‰), possibly through (1) the leaching of H_2S from magmatic lithologies and (2) the transport of metals and reduced sulfur rendered possible in moderate temperature magmatic-hydrothermal fluids (cf. [78]) (see next section). Thus, in the complex hydrodynamics of the restricted basin of the Helena Embayment, we contend that sulfur isotopic signatures of chalcopyrite clustering around 0‰ could identify a magmatic source of reduced sulfur in areas of Cu mineralization where evidence lack that barite was reductively dissolved to yield reduced sulfur for Cu mineralization.

5.3. Origin of Copper Mineralization. We propose that copper mineralization at Black Butte resulted from (1) a dominantly magmatic-hydrothermal metal source with subsidiary derivation of metals during thermally forced shale diagenesis and (2) flow of highly metalliferous reduced fluids within the shale sequence. Considering a timing for chalcopyrite mineralization at 1,488 ± 34 Ma overlapping with the revised age of the Newland Formation possibly older than 1,475 Ma [7, 21], we suggest that Cu mineralization was coeval with the timing of an enhanced thermal gradient in the Helena Embayment, possibly triggered by the NW-trending dike swarm that intruded into the Archean basement rocks to the south of the Helena Embayment until ca. 1,455 Ma [12, 15].

The unradiogenic to low radiogenic initial $^{187}Os/^{188}Os$ ratio for chalcopyrite (0.11 to 0.24) reflects that metals were brought by magmatic-hydrothermal seepages, possibly carrying H_2S credits with a magmatic sulfur signature in moderate-temperature magmatic-hydrothermal fluids. Fluid inclusion microthermometry studies in gangue minerals (quartz, barite, and dolomite) at Black Butte identified moderately saline mineralizing fluids (~15 wt.% NaCl equiv.; [34]). Moderate-temperature, reduced fluids with moderate salinities are able to transport barium, metals (i.e., Cu), and reduced sulfur at moderate temperature (>250°–350°C; [78, 79]). Such reduced fluids are likely to have been involved in chalcopyrite mineralization at Black Butte based on the buffering capacity of the host black shale.

At the Black Butte deposit, outside of the sulfide zones, no petrographic evidence exists for brittle-style veins or stockwork complexes that could have formed as the result of fluids introduced epigenetically in the Newland Formation (Tintina Montana, Inc., geologists, pers. comm., 2015). In a context of enhanced thermal gradient as described above, the converging effects of subsidence, forced diagenetic maturation, and compaction of shale sequences are known to contribute building up fluid overpressure needed for the flow of metal-bearing connate fluids in shale sequence [80, 81]. The continuous basin development and burial of hydrothermal vents proposed here for Black Butte [6, 7] could have triggered the necessary heat flow that has been proven elsewhere to facilitate fluid-rock equilibration, enhance diagenetic maturation and metal solubility (especially Cu) from shale source rock, and act as a driver of fluid advection in shale basins [81]. In this context, a subsidiary derivation of metals such as Cu and Os from the crustal shale sequence itself could rationally explain the possibly low radiogenic $^{187}Os/^{188}Os$ initial ratio of chalcopyrite up to 0.24. The present interpretation of reduced, metalliferous magmatic-hydrothermal fluids underpinned by our new Re-Os data for chalcopyrite expands on the original suggestion by Graham et al. [7] that metalliferous hydrothermal fluids were sourced and circulated either through the basement or from deeper parts of the basin.

5.4. Trigger for Precipitation of Cu ± Co ± Ag Mineralization. In our model, Cu and metals were largely contributed by moderate-temperature, reduced magmatic-hydrothermal fluids carrying reduced sulfur species with a magmatic origin. A recognized trigger for sulfide precipitation from such fluids is cooling, possibly accompanied by saturation in reduced sulfur, which would depreciate the solubility of chalcopyrite [78]. Chalcopyrite mineralization replaced locally massive synsedimentary to early diagenetic pyrite units that promoted precipitation of chalcopyrite (i.e., a feature previously recognized at the Tharsis deposit in the Iberian Pyrite Belt; [82, 83]). This replacement likely occurred close to the sediment-water interface, i.e., an ideal locus where fluids could cool. The thermochemical reductive dissolution of diagenetic barite also took place below the sediment-water

interface. Therefore, a pool of reduced sulfur comprising massive pyrite and reductive dissolution of barite was readily available in this setting for magmatic-hydrothermal fluids (themselves carrying H_2S with a magmatic origin) to cool and contribute precipitation of chalcopyrite ([6]; this study). The paragenetic association of chalcopyrite, chlorite, quartz, and pyrite lacking significant credits of sphalerite (ZnS) and galena (PbS) indicates that either reduced sulfur contents in the mineralizing fluids did not reach saturation for galena and sphalerite [81], in particular within the Lower Sulfide Zone [7], or the system remained hot enough so that the solubility threshold for limited PbS and ZnS deposition was not reached.

Chalcopyrite precipitation took place after a peculiar mineralization stage comprising Co-bearing sulfarsenides and sulfosalts (i.e., cobaltite, glaucodot, alloclasite, and tennantite) that was bereft of sulfide phases [33]. We suggest that this early Co-Ni stage may have a different origin to the one presented above for chalcopyrite. Metalliferous black shales may be enriched in metals such as Ni, Cu, As, and Co that are tied in organometallic complexes [84, 85]. Sediment-equilibrated, saline, and sulfide-deficient fluids could promote the transport of significant concentrations of metals (Cu, Co, As, and Ni), given the intermediate oxygen fugacity and mildly acidic pH generally imposed on by shale source rocks for these metals (see [81]). Thus, we conceptualize that the early Co-Ni-sulfarsenide-sulfosalt stage was related to the forced diagenetic maturation of shale in the Newland Formation caused by the enhanced thermal gradient on the edge of the GFTZ. This enhanced thermal gradient would in turn facilitate the release of acidic, saline, and sulfide-deficient fluids that would leach metals from organometallic complexes indigenous to shale in the Newland Formation.

6. Summary and Perspectives

Based on textural relationships and isotopic data presented in this study, several key features explain the origin of the Black Butte Cu sulfide mineralization hosted by black shale interbedded with sedimentary to early diagenetic massive pyrite units of the ca. >1,475 Ma Newland Formation in the Helena Embayment of the Mesoproterozoic Belt-Purcell Basin. Chalcopyrite formed at 1,488 ± 34 Ma (Re-Os isochron age) and most likely qualifies as a synsedimentary to diagenetic mineralization overlapping in time and space with formation of massive pyrite units. Copper mineralization at Black Butte is related to magmatic-hydrothermal activity on the edge of the Great Falls Tectonic Zone and an enhanced thermal gradient in possible connection with intrusion of dyke swarms until ca. 1,455 Ma. The initial $^{187}Os/^{188}Os$ isotopic composition of chalcopyrite (0.13 ± 0.11) is compatible with (1) derivation of Os from a markedly magmatic source with a $^{187}Os/^{188}Os$ isotopic composition inherited from the primitive upper mantle in the Mesoproterozoic ($Os_{mantle\ 1,475=}\ 0.12 \pm 0.02$) and (2) limited contamination from a continental crustal source with an estimated $^{187}Os/^{188}Os$ isotopic composition of 0.30 ± 0.23 that could cause an increase of initial $^{187}Os/^{188}Os$ ratios for chalcopyrite up to 0.24. This evidence favors a magmatic-hydrothermal metal source with subsidiary derivation of metals during thermally forced shale diagenesis and flow of highly metalliferous reduced fluids within the shale sequence.

Reduced, magmatic fluids with moderately high salinities probably transported metals (i.e., Cu) and reduced sulfur at moderate temperature (>250°–350°C) while buffered by the capacity of the host black shale. As magmatic-hydrothermal fluids cooled close to and below the sediment-water interface, chalcopyrite mineralization either (1) replaced locally massive synsedimentary to early diagenetic pyrite units, (2) used reduced sulfur species produced by thermochemical reductive dissolution of diagenetic barite, or (3) utilized the magmatic source of reduced sulfur in the moderate-temperature fluids in areas where Cu mineralization has sulfur isotope signatures clustering around 0‰ and did not proceed from reductive dissolution of barite.

In light of the work by Graham et al. [7], Present et al. [6] and the present contribution, it appears that critical controls on the genesis and metal endowment of stratiform Cu ± Co sulfide deposits in Mesoproterozoic shale sequences are (1) the presence of long-lived tectonic features like the Great Fall Tectonic Zone able to focus magmatic-hydrothermal fluid flow and permit intrusion of dyke swarms, (2) the impact of an enhanced thermal gradient on the thermal maturity of basinal rocks, and (3) the dynamics of bottom water with transient ingress of sulfate-bearing seawater in unconsolidated sediments governing the activity and health of microorganism communities at the loci of metalliferous hydrothermal venting. Finally, it has been shown that the continental crust had become particularly enriched in copper through Paleoproterozoic and Mesoproterozoic magmatic activity [86–88]. Future research building on the findings for the Black Butte deposit might demonstrate that the preponderance of strata-bound massive pyrite deposits with economic concentrations of base metals (Cu-Zn-Pb) within Mesoproterozoic strata is related to enhanced magmatic activity globally during this era.

Data Availability

All data are available in the manuscript file, the tables, figures and supplementary materials.

Disclosure

Nicolas J. Saintilan's present address is Institute of Geochemistry and Petrology, Department of Earth Sciences, ETH Zürich, Clausiusstrasse 25, 8092 Zürich, Switzerland (nicolas.saintilan@erdw.ethz.ch).

Conflicts of Interest

The authors declare that they have no conflicts of interest.

Authors' Contributions

NJS and RAC designed the study during field season 2015 while hosted by Tintina Montana Inc. and its Senior Vice President JZ. NJS carried out petrographic observations,

mineral separation, and sulfide and shale Re-Os isotope geochemistry procedures and mass spectrometry analyses, with contribution by RAC for several pyrite Re-Os analyses. TES and NJS ran the finite mixture modeling, with contribution by CCM. AB ran sulfur isotope geochemistry on samples provided by NJS. NJS wrote the manuscript with comments by all other authors. All authors reviewed and approved the manuscript.

Acknowledgments

This work was supported financially through Swiss National Science Foundation Early & Advanced Postdoc.Mobility Grants (#P2GEP2_162075 and #P300P2_171496) awarded to N.J. Saintilan (NJS). R.A. Creaser (RAC) acknowledges support from a NSERC Discovery Grant, Canada. D. Selby (DS) acknowledges the TOTAL Endowment Fund and Dida Scholarship of CUG Wuhan. NJS and DS also acknowledge the technical support of Antonia Hofmann, Dr. Geoff Nowell, and Dr. Chris Ottley. NJS and RAC are indebted to Tintina Montana, Inc., for access to their property and drill cores, as well as for fruitful discussions and a warm welcome. John F. Slack (Emeritus Scientist at the U.S. Geological Survey) is thanked for his comments and suggestions on an earlier version of the present article. We acknowledge the thorough reviews by Prof. Dr. Y. Zheng and Prof. Dr. Y. Li. Dr. J. Rowland is also thanked for the overall editorial handling.

Supplementary Materials

Supplementary 1. Supplementary Figure 1 statistical regression and Monte Carlo simulation for pyrite in cluster 1. See text for details.

Supplementary 2. Supplementary Figure 2 statistical regression and Monte Carlo simulation for chalcopyrite in cluster 1. See text for details.

Supplementary 3. Supplementary Figure 3 statistical regression and Monte Carlo simulation for pyrite in cluster 2. See text for details.

References

[1] J. W. Lydon, "Geology and metallogeny of the Belt-Purcell Basin," in *Mineral Deposits of Canada: A Synthesis of Major Deposit Types, District Metallogeny, the Evolution of Geological Provinces, and Exploration Methods*, W. D. Goodfellow, Ed., vol. 5, pp. 581–607, Geological Association of Canada, Mineral Deposits Division, Special Publication, 2007.

[2] J. Farquhar, N. Wu, D. E. Canfield, and H. Oduro, "Connections between sulfur cycle evolution, sulfur isotopes, sediments, and base metal sulfide deposits," *Economic Geology*, vol. 105, no. 3, pp. 509–533, 2010.

[3] R. J. Goldfarb, D. Bradley, and D. L. Leach, "Secular variation in economic geology," *Economic Geology*, vol. 105, no. 3, pp. 459–465, 2010.

[4] J. W. Lydon, "Sedimentary exhalative sulphides (SEDEX)," in *Geology of Canadian Mineral Deposit Types*, O. R. Eckstrand, W. D. Sinclair, and R. I. Thorpe, Eds., vol. 8, pp. 130–152, Geological Survey of Canada, Geology of Canada, 1996.

[5] T. W. Lyons, A. M. Gellatly, P. J. McGoldrick, and L. C. Kah, "Proterozoic sedimentary exhalative (SEDEX) deposits and links to evolving global ocean chemistry," in *Evolution of Early Earth's Atmosphere, Hydrosphere, and Biosphere—Constraints from Ore Deposits: Geological Society of America Memoir*, S. E. Kesler and H. Ohmoto, Eds., vol. 198, pp. 169–184, Geological Society of America, 2006.

[6] T. M. Present, K. D. Bergmann, C. Myers et al., "Pyrite-walled tube structures in a Mesoproterozoic sediment-hosted metal sulfide deposit," *Geological Society of America Bulletin*, vol. 130, no. 3-4, pp. 598–616, 2018.

[7] G. Graham, M. W. Hitzman, and J. Zieg, "Geologic setting, sedimentary architecture, and paragenesis of the Mesoproterozoic sediment-hosted Sheep Creek Cu-Co-Ag deposit, Helena Embayment, Montana," *Economic Geology*, vol. 107, no. 6, pp. 1115–1141, 2012.

[8] J. E. Harrison, "Precambrian Belt Basin of northwestern United States: its geometry, sedimentation and copper occurrences," *Geological Society of America Bulletin*, vol. 83, no. 5, pp. 1215–1240, 1972.

[9] T. W. Lyons, J. J. Luepke, M. E. Schreiber, and G. A. Zieg, "Sulfur geochemical constraints on Mesoproterozoic restricted marine deposition: Lower Belt Supergroup, northwestern United States," *Geochimica et Cosmochimica Acta*, vol. 64, pp. 427–437, 2000.

[10] D. T. Maxwell and J. Hower, "High-grade diagenesis and low-grade metamorphism of illite in the Precambrian Belt series," *American Mineralogist*, vol. 52, pp. 843–857, 1967.

[11] J. Schieber, "Pyrite mineralization in microbial mats from the mid-Proterozoic Newland Formation, Belt Supergroup, Montana, U.S.A.," *Sedimentary Geology*, vol. 64, no. 1-3, pp. 79–90, 1989.

[12] R. A. Price and J. W. Sears, "A preliminary palinspastic map of the Mesoproterozoic Belt-Purcell Supergroup, Canada and USA: implications for the tectonic setting and structural evolution of the Purcell anticlinorium and the Sullivan deposits," in *The Geological Environment of the Sullivan Deposit*, J. W. Lydon, T. Höy, J. F. Slack, and M. E. Knapp, Eds., vol. 1, pp. 61–81, Geological Association of Canada, Mineral Deposits Division, Special Publication, British Columbia, 2000.

[13] A. R. Nordsvan, W. J. Collins, Z. X. Li et al., "Laurentian crust in Northeast Australia: implications for the assembly of the supercontinent Nuna," *Geology*, vol. 46, no. 3, pp. 251–254, 2018.

[14] S. A. Pisarevsky, S. Å. Elming, L. J. Pesonen, and Z. X. Li, "Mesoproterozoic paleogeography: supercontinent and beyond," *Precambrian Research*, vol. 244, pp. 207–225, 2014.

[15] J. L. Wooden, C. J. Vitaliano, S. W. Koehler, and P. C. Ragland, "The late Precambrian mafic dikes of the southern Tobacco Root Mountains, Montana: geochemistry, Rb-Sr geochronology and relationships to Belt tectonics," *Canadian Journal of Earth Sciences*, vol. 15, pp. 467–479, 1978.

[16] J. F. Slack, L. A. Neymark, R. J. Moscati et al., "Origin of tin mineralization in the Sullivan Pb-Zn-Ag deposit, British Columbia: constraints from textures, geochemistry, and LA-ICP-MS U-Pb geochronology of cassiterite," *Economic Geology*, vol. 115, no. 8, pp. 1699–1724, 2020.

[17] H. E. Anderson and D. W. Davis, "U-Pb geochronology of the Moyie sills, Purcell Supergroup, southeastern British

Columbia: implications for the Mesoproterozoic geological history of the Purcell (Belt) Basin," *Canadian Journal of Earth Sciences*, vol. 32, no. 8, pp. 1180–1193, 1995.

[18] H. E. Anderson and R. R. Parrish, "U-Pb geochronological evidence for the geological history of the Belt-Purcell Supergroup, southeastern British Columbia," in *The Geological Environment of the Sullivan Deposit, British Columbia: Geological Association of Canada, Mineral Deposits Division*, J. W. Lydon, T. Höy, J. F. Slack, and M. Knapp, Eds., pp. 113–126, Special Publication, 2000.

[19] K. V. Evans, J. N. Aleinikoff, J. D. Obradovich, and M. C. Fanning, "SHRIMP U-Pb geochronology of volcanic rocks, Belt Supergroup, western Montana: evidence for rapid deposition of sedimentary strata," *Canadian Journal of Earth Sciences*, vol. 37, no. 9, pp. 1287–1300, 2000.

[20] J. W. Lydon, "A synopsis of the current understanding of the geological environment of the Sullivan deposit," in *The Geological Environment of the Sullivan Pb-Zn-Ag deposit, British Columbia*, J. W. Lydon, T. Höy, J. F. Slack, and M. Knapp, Eds., vol. 1, pp. 12–31, Geological Association of Canada, Mineral Deposits Division, Special Publication, 2000.

[21] J. Perelló, J. A. Clifford, A. J. Wilson, S. Kennedy, R. A. Creaser, and V. A. Valencia, "On the timing and metallogenic implications of the sediment-hosted copper-silver mineralization in the Creston Formation (Belt-Purcell Supergroup), British Columbia, Canada," *Ore Geology Reviews*, vol. 131, no. article 104032, 2021.

[22] F. W. Chandler and G. A. Zieg, *Was the depositional environment of the Sullivan Zn-Pb deposit in British Columbia marine or lacustrine and how saline was it? A summary of the data*, Current Research Paper 1994-A, Geological Survey of Canada, 1994.

[23] G. A. Zieg, "Stratigraphy and sedimentology of the Middle Proterozoic upper Newland Limestone," in *Belt Supergroup: A guide to the Proterozoic rocks of Western Montana and adjacent areas*, S. M. Roberts, Ed., vol. 94, pp. 125–141, Montana Bureau of Mines and Geology Special Publication, 1986.

[24] T. Algeo, G. Luo, H. Song, T. Lyons, and D. Canfield, "Reconstruction of secular variation in seawater sulfate concentrations," *Biogeosciences*, vol. 12, no. 7, pp. 2131–2151, 2015.

[25] N. J. Planavsky, P. McGoldrick, C. T. Scott et al., "Widespread iron-rich conditions in the mid-Proterozoic ocean," *Nature*, vol. 477, no. 7365, pp. 448–451, 2011.

[26] S. P. Slotznick, J. Zieg, S. M. Webb, J. L. Kirschvink, and W. W. Fischer, "Iron mineralogy and redox chemistry of the Mesoproterozoic Newland Formation in the Helena Embayment, Belt Supergroup, Montana," *Northwest Geology*, vol. 44, pp. 55–72, 2015.

[27] D. F. Sangster, "The role of dense brines in the formation of vent-distal sedimentary-exhalative (SEDEX) lead-zinc deposits: field and laboratory evidence:," *Mineralium Deposita*, vol. 37, pp. 149–157, 2002.

[28] T. W. Lyons, T. D. Frank, M. E. Schreiber, D. Winston, and K. C. Lohmann, "Geochemical constraints on paleoenvironments within the Belt Supergroup (Middle Proterozoic), Montana," in *Belt Symposium III*, R. B. Berg, Ed., vol. 112, pp. 190–201, Montana Bureau of Mines and Geology Special Publication, 1993.

[29] H. Strauss and J. Schieber, "A sulfur isotope study of pyrite genesis: The mid-proterozoic Newland formation, belt supergroup, Montana," *Geochimica et Cosmochimica Acta*, vol. 54, no. 1, pp. 197–204, 1990.

[30] B. B. Jørgensen, "A theoretical model of the stable sulfur isotope distribution in marine sediments," *Geochimica et Cosmochimica Acta*, vol. 43, no. 3, pp. 363–374, 1979.

[31] S. K. Juniper, I. R. Jonasson, V. Tunnicliffe, and A. J. Southward, "Influence of a tube-building polychaete on hydrothermal chimney mineralization," *Geology*, vol. 20, no. 10, pp. 895–898, 1992.

[32] J. Schieber, "Marcasite in black shales—a mineral proxy for oxygenated bottom waters and intermittent oxidation of carbonaceous muds," *Journal of Sedimentary Research*, vol. 81, no. 7, pp. 447–458, 2011.

[33] J. White, C. H. Gammons, and G. A. Zieg, "Paragenesis of cobalt and nickel in the Black Butte shale-hosted copper deposit, Belt Basin, Montana, USA," *Mineralium Deposita*, vol. 49, no. 3, pp. 335–351, 2014.

[34] G. A. Zieg, C. H. B. Leitch, and R. B. Berg, "The geology of the sheep creek copper deposits, Meagher County, Montana," in *MBMG Open-File Report 381*, pp. 67–69, Montana Bureau of Mines and Geology, Butte, 1999.

[35] A. M. Gellatly and T. W. Lyons, "Trace sulfate in mid-Proterozoic carbonates and the sulfur isotope record of biospheric evolution," *Geochimica et Cosmochimica Acta*, vol. 69, no. 15, pp. 3813–3829, 2005.

[36] H. Strauss, "The sulfur isotopic record of Precambrian sulfates: new data and a critical evaluation of the existing record," *Precambrian Research*, vol. 63, no. 3-4, pp. 225–246, 1993.

[37] G. A. Zieg and C. H. B. Leitch, "The geology of the Sheep Creek copper deposit, Meagher County, Montana," in *Belt Symposium III*, pp. 2–4, Informal Program and Abstracts, Whitefish, Montana, 1993.

[38] R. R. Seal II, "Sulfur isotope geochemistry of sulfide minerals," *Reviews in Mineralogy and Geochemistry*, vol. 61, no. 1, pp. 633–677, 2006.

[39] N. J. Saintilan, R. A. Creaser, and A. A. Bookstrom, "Re-Os systematics and geochemistry of cobaltite (CoAsS) in the Idaho cobalt belt, Belt-Purcell Basin, USA: Evidence for middle Mesoproterozoic sediment- hosted Co-Cu sulfide mineralization with Grenvillian and Cretaceous remobilization," *Ore Geology Reviews*, vol. 86, pp. 509–525, 2017.

[40] J. Schieber, "The origin and economic potential of sandstone-hosted disseminated Pb-Zn mineralization in pyritic shale horizons of the mid-Proterozoic Newland Formation, Montana, USA," *Mineralium Deposita*, vol. 26, pp. 290–297, 1991.

[41] P. T. Doughty and K. R. Chamberlain, "Salmon River arch revisited: New evidence for 1370 Ma rifting near the end of deposition in the Middle Proterozoic Belt Basin," *Canadian Journal of Earth Sciences*, vol. 33, no. 7, pp. 1037–1052, 1996.

[42] S. B. Shirey and R. J. Walker, "Carius tube digestion for low-blank rhenium-osmium analysis," *Analytical Chemistry*, vol. 67, no. 13, pp. 2136–2141, 1995.

[43] D. Selby, K. D. Kelley, M. W. Hitzman, and J. Zieg, "Re-Os SULFIDE (bornite, chalcopyrite, and pyrite) systematics of the carbonate-hosted copper deposits at Ruby Creek, southern Brooks Range, Alaska," *Economic Geology*, vol. 104, no. 3, pp. 437–444, 2009.

[44] V. M. Cumming, D. Selby, and P. G. Lillis, "Re-Os geochronology of the lacustrine Green River Formation: insights into direct depositional dating of lacustrine successions, Re-Os systematics and paleocontinental weathering," *Earth and Planetary Science Letters*, vol. 359-360, pp. 194–205, 2012.

[45] R. A. Creaser, D. A. Papanastassiou, and G. J. Wasserburg, "Negative thermal ion mass spectrometry of osmium, rhenium and iridium," *Geochimica et Cosmochimica Acta*, vol. 55, no. 1, pp. 397–401, 1991.

[46] J. Völkening, T. Walczyk, and K. Heumann, "Osmium isotopic ratio determination by negative thermal ionization mass spectrometry," *International Journal of Spectrometric Ionic Physics*, vol. 105, pp. 147–159, 1991.

[47] B. W. Robinson and M. Kusakabe, "Quantitative preparation of sulfur dioxide, for sulfur-34/sulfur-32 analyses, from sulfides by combustion with cuprous oxide," *Analytical Chemistry*, vol. 47, no. 7, pp. 1179–1181, 1975.

[48] J. H. F. L. Davies, T. E. Sheldrake, J. R. Reimink, J.-F. Wotzlaw, C. Moeck, and A. Finlay, "Investigating complex isochron data using mixture models," *Geochemistry, Geophysics, Geosystems*, vol. 19, no. 10, pp. 4035–4047, 2018.

[49] F. Leisch, "Flexmix: a general framework for finite mixture models and latent glass regression in R," *Journal of Statistical Software*, vol. 11, pp. 1–18, 2004.

[50] K. Ludwig, *ISOPLOT, version 4.15: a geochronological toolkit for Microsoft Excel*, Berkeley Geochronology Center, Special Publication, Berkeley, California, 2011.

[51] M. I. Smoliar, R. J. Walker, and J. W. Morgan, "Re-Os ages of group IIA, IIIA, IVA, and IVB iron meteorites," *Science*, vol. 271, no. 5252, pp. 1099–1102, 1996.

[52] Y. Li, S. Zhang, R. Hobbs et al., "Monte Carlo sampling for error propagation in linear regression and applications in isochron geochronology," *Science Bulletin*, vol. 64, no. 3, pp. 189–197, 2019.

[53] R. W. Carlson, "Application of the Pt-Re-Os isotopic systems to mantle geochemistry and geochronology," *Lithos*, vol. 82, no. 3-4, pp. 249–272, 2005.

[54] T. Meisel, R. J. Walker, A. J. Irving, and J. P. Lorand, "Osmium isotopic compositions of mantle xenoliths," *A global perspective: Geochimica et Cosmochimica Acta*, vol. 65, pp. 1311–1323, 2001.

[55] D. Hnatyshin, R. A. Creaser, S. Meffre, R. A. Stern, J. J. Wilkinson, and E. C. Turner, "Understanding the microscale spatial distribution and mineralogical residency of Re in pyrite: Examples from carbonate-hosted Zn-Pb ores and implications for pyrite Re-Os geochronology," *Chemical Geology*, vol. 533, p. 119427, 2020.

[56] C. R. M. McFarlane, "A geochronological framework for sedimentation and Mesoproterozoic tectono-magmatic activity in lower Belt-Purcell rocks exposed west of Kimberley," *British Columbia: Canadian Journal of Earth Sciences*, vol. 52, pp. 444–465, 2015.

[57] M. E. McMechan and R. A. Price, "Superimposed low-grade metamorphism in the Mount Fisher area, southeastern British Columbia—implications for the East Kootenay orogeny," *Canadian Journal of Earth Sciences*, vol. 19, no. 3, pp. 476–489, 1982.

[58] N. A. Zirakparvar, J. D. Vervoort, W. McClelland, and R. S. Lewis, "Insights into the metamorphic evolution of the Belt-Purcell Basin: evidence from Lu-Hf garnet geochronology," *Canadian Journal of Earth Sciences*, vol. 47, pp. 161–179, 2010.

[59] J. N. Aleinikoff, J. F. Slack, K. Lund et al., "Constraints on the timing of Co-Cu+Au mineralization in the Blackbird district, Idaho, using SHRIMP U-Pb ages of monazite and xenotime plus zircon ages of related Mesoproterozoic orthogneisses and metasedimentary rocks," *Economic Geology*, vol. 107, no. 6, pp. 1143–1175, 2012.

[60] J. F. Slack, "Strata-bound Fe-Co-Cu-Au-Bi-Y-REE deposits of the Idaho cobalt belt: multistage hydrothermal mineralization in a magmatic-related iron oxide copper-gold system," *Economic Geology*, vol. 107, no. 6, pp. 1089–1113, 2012.

[61] D. Milidragovic, D. J. Thorkelson, W. J. Davis, D. D. Marshall, and H. D. Gibson, "Evidence for late Mesoproterozoic tectonism in northern Yukon and the identification of a Grenville-age tectonothermal belt in western Laurentia," *Terra Nova*, vol. 23, no. 5, pp. 307–313, 2011.

[62] T. O. Nesheim, J. D. Vervoort, W. C. McClelland, J. A. Gilotti, and H. M. Lang, "Mesoproterozoic syntectonic garnet within Belt Supergroup metamorphic tectonites: evidence of Grenville-age metamorphism and deformation along northwest Laurentia," *Lithos*, vol. 134, pp. 91–107, 2012.

[63] J. F. Slack, J. N. Aleinikoff, H. E. Belkin, C. M. Fanning, and P. W. Ransom, "Mineral chemistry and SHRIMP U-Pb geochronology of Mesoproterozoic polycrase-titanite veins in the Sullivan Pb-Zn-Ag deposit, British Columbia," *Canadian Mineralogist*, vol. 46, no. 2, pp. 361–378, 2008.

[64] Y. Li, D. Selby, X.-H. Li, and C. J. Ottley, "Multisourced metals enriched by magmatic-hydrothermal fluids in stratabound deposits of the Middle-Lower Yangtze River metallogenic belt, China," *Geology*, vol. 46, no. 5, pp. 391–394, 2018.

[65] N. J. Saintilan, A. D. Sproson, D. Selby et al., "Osmium isotopic constraints on sulphide formation in the epithermal environment of magmatic-hydrothermal mineral deposits," *Chemical Geology*, vol. 564, p. 120053, 2021.

[66] K. Chen, R. J. Walker, R. L. Rudnick et al., "Platinum-group element abundances and Re-Os isotopic systematics of the upper continental crust through time: evidence from glacial diamictites," *Geochimica et Cosmochimica Acta*, vol. 191, pp. 1–16, 2016.

[67] W. R. Keefer, *Geologic map of the west half of the Neihart 15-minute quadrangle, central Montana*, U.S. Geological Survey Miscellaneous Investigations Series Map I-276, scale 1:62'500, USGS Publications Warehouse, 1972.

[68] C. D. Walcott, "Pre-Cambrian fossiliferous formations," *Geological Society of America Bulletin*, vol. 10, no. 1, pp. 199–244, 1899.

[69] D. E. Boerner, J. A. Craven, R. D. Kurtz, G. M. Ross, and F. W. Jones, "The Great Falls tectonic zone: suture or intracontinental shear zone?," *Canadian Journal of Earth Sciences*, vol. 35, no. 2, pp. 175–183, 1998.

[70] J. N. Gifford, P. A. Mueller, D. A. Foster, and D. W. Mogk, "Extending the realm of Archean crust in the Great Falls tectonic zone: evidence from the Little Rocky Mountains, Montana," *Precambrian Research*, vol. 315, pp. 264–281, 2018.

[71] A. Gorman, R. Clowes, R. Ellis et al., "Deep probe: imaging the roots of western North America," *Canadian Journal of Earth Sciences*, vol. 39, no. 3, pp. 375–398, 2002.

[72] P. A. Mueller, A. L. Heatherington, D. M. Kelly, J. L. Wooden, and D. W. Mogk, "Paleoproterozoic crust within the Great Falls tectonic zone: implications for the assembly of southern Laurentia," *Geology*, vol. 30, no. 2, pp. 127–130, 2002.

[73] P. A. Mueller, H. Burger, J. Wooden et al., "Paleoproterozoic metamorphism in the northern Wyoming Province: implications for the assembly of Laurentia," *Journal of Geology*, vol. 133, pp. 169–179, 2005.

[74] P. A. Mueller, D. W. Mogk, J. Wooden, and D. Spake, "U-Pb ages of zircons from the Lower Belt Supergroup and proximal crystalline basement: implications for the early evolution of the Belt Basin," *Geological Society of America Special Paper*, vol. 522, 2016.

[75] J. O'Neil and D. Lopez, "Character and regional significance of Great Falls tectonic zone, east-central Idaho and west-central Montana," *American Association of Petroleum Geology Bulleting*, vol. 69, pp. 437–447, 1985.

[76] R. W. Carlson and A. J. Irving, "Depletion and enrichment history of subcontinental lithospheric mantle: An Os, Sr, Nd and Pb isotopic study of ultramafic xenoliths from the northwestern Wyoming Craton," *Earth and Planetary Science Letters*, vol. 126, no. 4, pp. 457–472, 1994.

[77] R. E. Zartman, "Archean crustal lead in the Helena Embayment of the Belt Basin," in *Basement Tectonics 8: Characterization and Comparison of Ancient and Mesozoic Continental Margins*, Proceedings of the 8th International Conference on Basement Tectonics (Butte, Montana), M. J. Bartholomew, D. W. Hyndman, D. W. Mogk, and R. Mason, Eds., pp. 699–710, Kluwer Academic Publishers, Dordrecht, The Netherlands, 1989.

[78] R. Zhong, J. Brugger, Y. Chen, and W. Li, "Contrasting regimes of Cu, Zn and Pb transport in ore-forming hydrothermal fluids," *Chemical Geology*, vol. 395, pp. 154–164, 2015.

[79] Z. Xiao, C. H. Gammons, and A. E. Williams-Jones, "Experimental study of copper(I) chloride complexing in hydrothermal solutions at 40 to 300°C and saturated water vapor pressure," *Geochimica et Cosmochimica Acta*, vol. 62, no. 17, pp. 2949–2964, 1998.

[80] J. W. Lydon, "Chemical parameters controlling the origin and deposition of sediment-hosted stratiform lead-zinc deposits," in *Sediment-Hosted Stratiform Lead-Zinc Deposits: Mineralogical Association of Canada, vol 9*, Short Course Handbook, D. F. Sangster, Ed., pp. 175–250, Mineralogical Association of Canada, 1983.

[81] F. Tornos and C. A. Heinrich, "Shale basins, sulfur-deficient ore brines and the formation of exhalative base metal deposits," *Chemical Geology*, vol. 247, no. 1-2, pp. 195–207, 2008.

[82] E. Marcoux and J. M. Leistel, "Mineralogy and geochemistry of massive sulphide deposits," *Iberian Pyrite Belt: Boletin Geologico Minero*, vol. 107, pp. 117–126, 1996.

[83] F. Tornos, E. Gonzalez Clavijo, and E. F. Spiro, "The Filon Norte orebody (Tharsis, Iberian Pyrite Belt): a proximal low-temperature shale-hosted massive sulphide in a thin-skinned tectonic belt," *Mineralium Deposita*, vol. 72, pp. 175–192, 1998.

[84] D. A. C. Manning and A. P. Giże, "The role of organic matter in ore transport processes," in *Organic Geochemistry: Topics in Geobiology*, M. H. Engel and S. A. Macko, Eds., vol. 11, pp. 547–563, Springer, Boston, MA, 1993.

[85] J. F. Slack, D. Selby, and J. A. Dumoulin, "Hydrothermal, Biogenic, and Seawater Components in Metalliferous Black Shales of the Brooks Range, Alaska: Synsedimentary Metal Enrichment in a Carbonate Ramp Setting," *Economic Geology*, vol. 110, no. 3, pp. 653–675, 2015.

[86] P. Kaur and N. Chaudhri, "Metallogeny associated with the Palaeo-Mesoproterozoic Columbia supercontinent cycle: a synthesis of major metallic deposits," *Ore Geology Reviews*, vol. 56, pp. 415–422, 2014.

[87] Z. X. Li, S. V. Bogdanova, A. S. Collins et al., "Assembly, configuration, and break-up history of Rodinia: A synthesis," *Precambrian Research*, vol. 160, no. 1-2, pp. 179–210, 2008.

[88] J. Parnell and A. J. Boyce, "Neoproterozoic copper cycling, and the rise of metazoans," *Scientific Reports*, vol. 9, no. 1, p. 3638, 2019.

[89] S. V. Arkadkskyi, R. A. Creaser, J. P. Richards, D. Hnatyshin, and L. Hardy, "Re-Os dating of arsenopyrite from the Galena mine — evidence for Mesoproterozoic age of the Ag-Pb-Zn mineralization in the Coeur d'Alene district," *Idaho: Geological Society of America, Program with Abstracts*, vol. 41, p. 83, 2009.

[90] K. Lund, J. N. Aleinikoff, M. Kunk et al., "SHRIMP U-Pb and $^{40}Ar/^{39}Ar$ Age constraints for relating plutonism and mineralization in the Boulder batholith region, Montana," *Economic Geology*, vol. 97, no. 2, pp. 241–267, 2002.

[91] J. H. Dilles, M. W. Martin, H. Stein, and B. Rusk, "Re-Os and U-Pb ages for the Butte copper district, Montana: a short- or long-lived hydrothermal system?," *Geological Society of America, Program with Abstracts*, vol. 35, p. 400, 2003.